iScience

CellPress
OPEN ACCESS

Article

Lymph Node Subcapsular Sinus Microenvironment-On-A-Chip Modeling Shear Flow Relevant to Lymphatic Metastasis and Immune Cell Homing

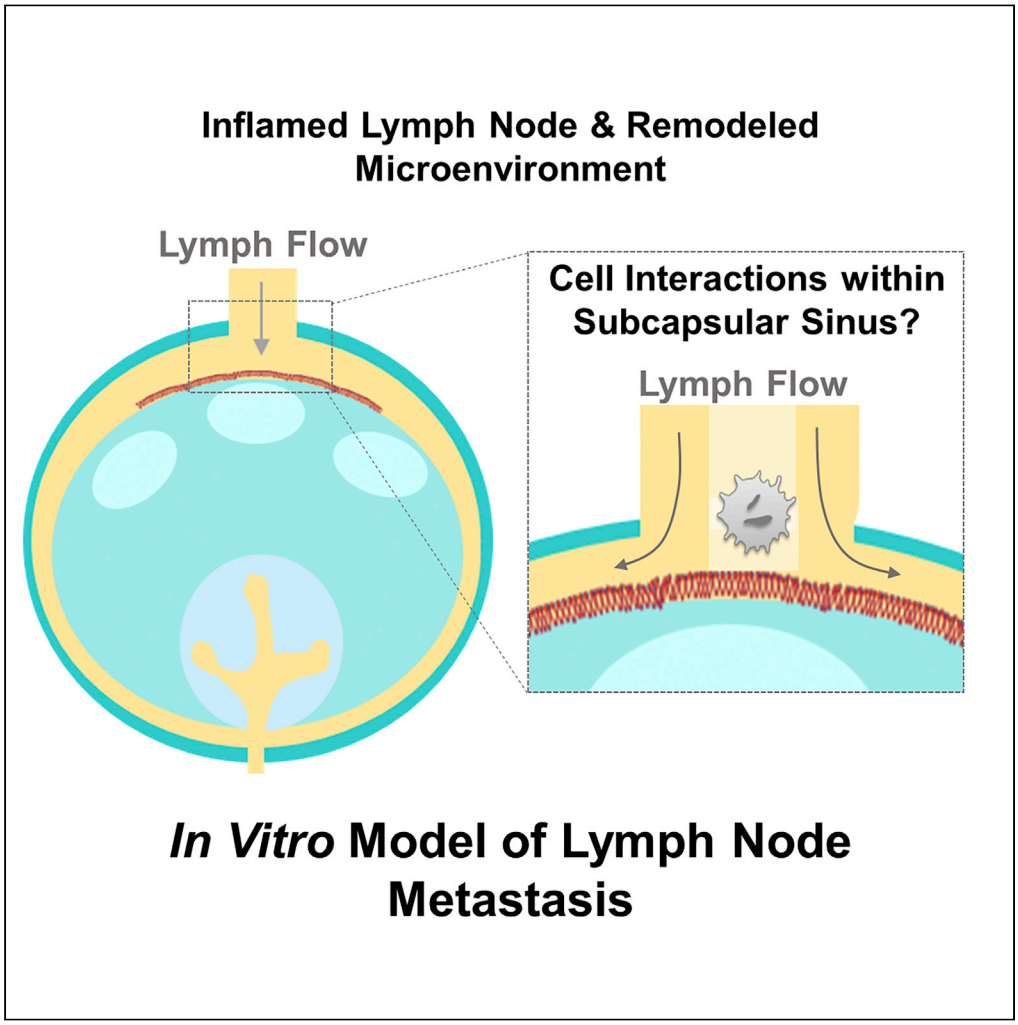

Katherine G. Birmingham, Meghan J. O'Melia, Samantha Bordy, David Reyes Aguilar, Bassel El-Reyas, Gregory Lesinski, Susan N. Thomas

susan.thomas@gatech.edu

HIGHLIGHTS

A lymph node subcapsular sinus-on-a-chip was engineered to study lymphatic metastasis

Altered fluid flows and adhesive ligands regulate cell adhesion in subcapsular sinus

Monocytes increase cancer cell adhesion adhesion in a lymph node flow-dependent manner

Biophysical effects of lymph node remodeling regulates lymphatic metastasis mechanisms

Birmingham et al., iScience *23*, 101751
November 20, 2020
https://doi.org/10.1016/j.isci.2020.101751

iScience

CellPress
OPEN ACCESS

Article

Lymph Node Subcapsular Sinus Microenvironment-On-A-Chip Modeling Shear Flow Relevant to Lymphatic Metastasis and Immune Cell Homing

Katherine G. Birmingham,[1,2] Meghan J. O'Melia,[3] Samantha Bordy,[1] David Reyes Aguilar,[1,2] Bassel El-Reyas,[4] Gregory Lesinski,[4] and Susan N. Thomas[1,2,3,4,5,*]

SUMMARY

A lymph node sinus-on-a-chip adhesion microfluidic platform that recapitulates the hydrodynamic microenvironment of the lymph node subcapsular sinus was engineered. This device was used to interrogate the effects of lymph node remodeling on cellular adhesion in fluid flow relevant to lymphatic metastasis. Wall shear stress levels analytically estimated and modeled after quiescent and diseased/inflamed lymph nodes were experimentally recapitulated using a flow-based microfluidic perfusion system to assess the effects of physiological flow fields on human metastatic cancer cell adhesion. Results suggest that both altered fluid flow profiles and presentation of adhesive ligands, which are predicted to manifest within the lymph node subcapsular sinus as a result of inflammation-induced remodeling, and the presence of lymph-borne monocytic cells may synergistically contribute to the dynamic extent of cell adhesion in flow relevant to lymph node invasion by cancer and monocytic immune cells during lymphatic metastasis.

INTRODUCTION

The presence of cancerous cells in the lymph node (LN) negatively correlates with patient survival in many cancer types (Fortea-Sanchis et al., 2018; Pai et al., 2011; You et al., 2019). Yet as many as 45% of patients have LN involvement, and a startling 89% have disseminated tumor cells within their LNs in the context of colon and pancreatic cancers, respectively (Weledji et al., 2016; Wong, 2009). Although still debated (Wong and Hynes, 2006), the general hypothesis underlying how LN metastasis occurs is that the lymphatic vasculature provides a conduit for invasive cancer cell movement to LNs through a process likely facilitated by both chemotactic cues and fluid flows driven by lymph propulsion. Once in LNs, metastatic cells can undergo extensive interactions with resident immune cells that influence their metastatic behavior. In particular, it is known that immune tolerance is associated with metastatic spread as well as drug resistance (Makkouk and Weiner, 2015; Vinay et al., 2015). Understanding the interactions of metastatic cells within this anatomical location, which has been widely implicated in influencing anti-tumor immunity and response to therapy, is thus of high relevance to treating cancer, including that of the colon and pancreas, in the current immunotherapy era. In addition, a therapeutic window has been proposed wherein systemic dissemination of metastatic disease can be ameliorated (Fontebasso and Dubinett, 2015). In such a context, understanding the biology underlying lymphatic metastasis has the potential to identify unique druggable targets for cancers that have spread to LNs.

Transit via the lymphatic system has the potential to provide lymph-borne cancer cells access to the systemic circulation in two manners. First, lymphatic vessels return lymph and its contents to blood at the thoracic duct (Moore and Bertram, 2018). However, numerous reports have demonstrated the potential for a second, perhaps more likely, dissemination route. This may occur via invasion within the local LN microenvironment and access by LN parenchyma-resident cancer cells to the circulatory system at the LN's capillary network (Carr, 1983; Karaman and Detmar, 2014). Thus, the ability of lymph-borne cancer cells to recapitulate the lymphatic-mediated homing behaviors of immune cells (Boscacci et al., 2010) and arrest in LNs despite lymph flow and then transmigrate into the LN parenchyma may therefore contribute to metastatic dissemination through the lymphatic route. Notably, numerous reports have documented evidence of the accumulation of circulating tumor cells within the subcapsular sinus (SCS).

[1]George W. Woodruff School of Mechanical Engineering, Georgia Institute of Technology, Atlanta, GA 30332, USA

[2]Parker H. Petit Institute for Bioengineering and Bioscience, Georgia Institute of Technology, IBB 2310 315 Ferst Drive NW, Atlanta, GA 30332, USA

[3]Wallace H. Coulter Department of Biomedical Engineering, Georgia Institute of Technology and Emory University, Atlanta, GA 30332, USA

[4]Winship Cancer Institute, Emory University, Atlanta, GA 30322, USA

[5]Lead Contact

*Correspondence: susan.thomas@gatech.edu

https://doi.org/10.1016/j.isci.2020.101751

The subsequent invasion of these cells into the LN parenchyma can be blocked by inhibition of adhesion receptors (Jeong et al., 2019; Lee et al., 2013) or chemotactic cues (Ji, 2017). Together, the involvement of the LNs in the multifaceted progression of the metastatic cascade is thought to allow the formation of numerous, simultaneously occurring secondary tumors originating from a single primary tumor. However, the mechanisms by which this occurs remain essentially undefined.

As in the hematogenous context, metastasis by lymph-borne cells occurs within luminal flow fields driven by propulsive lymph flow (Sleeman et al., 2011; Wong and Hynes, 2006). The resulting hydrodynamic forces play essential roles in regulating adhesion relevant to metastatic extravasation (Moore and Bertram, 2018). Specifically, the dispersive effects of such hydrodynamic force must be overcome by adhesive interactions in order to enable receptor signaling and chemotaxis (Huang et al., 2018; Wirtz et al., 2011). Although volumetric flow rates of lymph are far lower than that in blood, the stress levels experienced within vessels are not dissimilar (Planas-Paz and Lammert, 2014). Thus, it could be expected that adhesive processes involved in immune cell homing and metastasis through the blood vasculature may be involved in regulating lymphatic dissemination. This is supported by observations of LN metastasis via the lymphatic route being inhibited by loss of function by cell adhesion receptors including, but not limited to, intracellular adhesion molecule (ICAM) and vascular adhesion molecule (VCAM) (Jeong et al., 2019; Kong et al., 2018) using genetic knockout models or antibody inhibition strategies. Moreover, lymphatic endothelial cells that line the interior of the LN SCS express cell adhesion molecules E- and P-selectin as well as ICAM and VCAM, among others, at levels that are dynamically responsive to inflammation state (Achen and Stacker, 2008; Habenicht et al., 2017; Hinson et al., 2017). In hemodynamic flow, ICAM and/or VCAM mediate cell arrest via a multistep process facilitated by selectin- and/or VCAM-mediated rolling adhesion (Jones et al., 1994; Yago et al., 1999; McCarty et al., 2000; Jadhav et al., 2001; Edwards and Thomas, 2017). How such SCS-presented adhesion molecules influence adhesive interactions by both cancer and immune cells in lymph-mimicking flow fields, however, has yet to be elaborated.

Concurrent with stromal cell and lymphocyte responses to disease and/or inflammation, LNs are widely reported to structurally remodel. A hallmark of metastatic disease is lymphadenopathy, i.e. swollen LNs (West and Jin, 2016). Concurrently, tissue stiffening can occur (Rohner et al., 2015; Swartz and Lund, 2012), which is often attributed to metastatic colonization, but conversely has been reported in LNs prior to metastasis (Miyaji et al., 1997; Paszek et al., 2005; Rohner et al., 2015). In addition to expansion of the LN parenchyma-localized fibroblastic reticulum (Riedel et al., 2016) and high endothelial venules (Webster et al., 2006), both afferent (LN-entering) lymphatic vessels and the SCS are known to dilate in contexts of human disease (McLaughlin et al., 2010; Pan et al., 2010; Seidl et al., 2018), effects that are also recapitulated in mouse models (Achen and Stacker, 2008; Habenicht et al., 2017; Hinson et al., 2017). How these changes have the potential to synergistically influence cell dissemination to LNs has not been systemically explored. This is hampered in large part by the reliance on mouse models that differ subtly from human LNs in their structures as well as the inability to uncouple biomolecular versus biophysical changes that often occur concurrently in states of disease using *in vivo* models.

To fill these critical gaps, we sought to bring *in vitro* tools long employed in the context of studying leukocyte adhesion and blood-borne metastasis to the problem of analyzing mechanisms of LN metastasis. Such microfluidic systems offer the advantage of enabling high-throughput experimentation under defined molecular, cellular, and/or biophysical conditions, thus substantially increasing the number of experimental conditions that can be explored (Edwards et al., 2017; Hanley et al., 2006; Thomas et al., 2008). Furthermore, coupling these microfluidic devices with high-speed videomicroscopy permits rapid and facile visualization and quantification of the adhesive behavior of thousands of cells in a single experiment to increase statistical robustness (Birmingham et al., 2020; Edwards et al., 2017, 2018; Oh et al., 2015). Using this "LN sinus-on-a-chip" adhesive microfluidic platform, we explored the effects of wall shear stress (WSS) magnitude and dissipation, which were modeled to occur within the LN SCS, on adhesion by cell types that disseminate to LNs via the lymphatic vasculature, including human metastatic colon and pancreatic carcinoma and monocytic cell lines. Our results demonstrate that the LN SCS flow microenvironment regulates the dependencies of E-selectin-enabled adhesion extent but not rolling velocity magnitude on WSS. As a result, overall levels of E-selectin-mediated metastatic and monocytic cell adhesion in the context of flow regimes modeled after inflamed relative to quiescent LNs are modulated by the extent of adhesion in the flow channel, an effect regulated interdependently by context of ICAM and/or VCAM co-presentation. This suggests the potential for structural changes within the SCS and afferent lymphatic vessel to influence

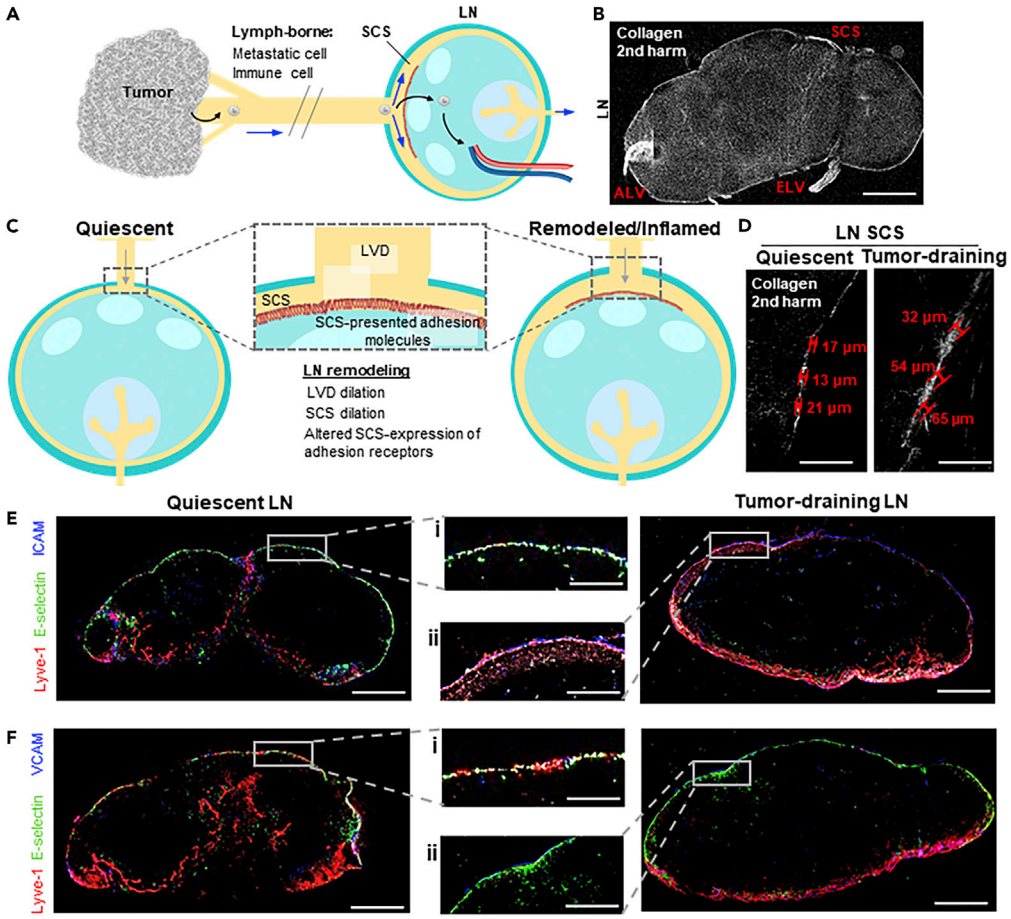

Figure 1. Metastatic Cancer and Immune Cells Traffic to Lymph Nodes (LNs) via Draining Lymphatic Vessels, Both of Which Remodel in States of Inflammation

(A) Invasive cancer cells and immune cells enter the local lymphatic drainage basin to gain access to and invade draining LNs. Blue arrows: directions of fluid drainage. Black arrows: potential metastatic cancer cell paths of invasion.

(B) Image of LN second harmonic (collagen). Scale bar, 400 μm.

(C) In tumor contexts or in states of inflammation, LNs remodel, a process that can include the dilation of the subcapsular sinus (SCS) and afferent lymphatic vessel (lymphatic vessel diameter, LVD) and alter adhesion molecule expression by sinus lining cells.

(D) Second harmonic images of quiescent (tumor-free) and LNs draining day 7 B16F10 tumor (tumor-draining). Red: SCS height measurements. Scale bars, 150 μm.

(E and F) Immunohistochemical staining for Lyve-1 (red), E-selectin (green), and either ICAM (E) or VCAM (F) (blue) within 8-μm thick sections of a quiescent (left) murine LN or LN draining day 7 B16F10 tumor (right). Scale bars, 400 (i) or 150 (ii) μm.

interactions of metastatic and immune cells within the LN SCS. Co-perfusion with monocytes, whose E-selectin enabled adhesion was similarly regulated by flow regime and adhesive ligand presentation, also increased metastatic cell adhesion in flow in a manner regulated by flow microenvironment, linking inflammation and mobilization of lymph-borne immune cells to the regulation of lymphatic metastasis. Our results implicate the biophysical effects of LN remodeling as a potential axis regulating the mechanisms of LN invasion negatively implicated in cancer patient outcomes.

RESULTS

Lymphatic Metastasis, LN Invasion, and LN Tissue Remodeling

Lymphatic metastasis is a multistep process (Figure 1A) wherein lymph-borne metastatic cells invade into LNs through the SCS, resulting in formation of LN tumors seen in human patients (Karaman and Detmar, 2014) as

well as metastatic mouse tumor models (Nakashima et al., 2011; Singh and Choi, 2019). LN structural features (Figures 1B and 1C) influence fluid flow paths and thus the movement of lymph-borne cells, including afferent lymphatic vessels and the SCS, which disperses lymph radially around the LN parenchyma (Jafarnejad et al., 2015; Moore and Bertram, 2018). In the context of disease or inflammation, these LN structures can be altered (Achen and Stacker, 2008; Habenicht et al., 2017; Hinson et al., 2017) to result in lymphatic vessel (Lund et al., 2016a; Nakayama et al., 1999) or SCS (Das et al., 2013; Ozasa et al., 2012; Sweety and Narayankar, 2019) dilation. Within this perfused microenvironment, cells lining the SCS wall express adhesion molecules (Figure 1C), including E-selectin, ICAM, and VCAM, that are known to synergistically mediate cell adhesion in the context of fluid flows (Kong et al., 2018; López et al., 1999). Expression of adhesion receptors by lymphatic endothelial cells, which line the SCS, is altered by shear stress and exposure to other inflammatory mediators (Kawai et al., 2012; Trevaskis et al., 2015; Yan et al., 2014). For example, the SCS is dilated in LNs draining mouse melanomas (Figure 1D), as cell adhesion molecules expressed within the SCS of these LNs remodel (Figures 1E and 1F). This is in line with reports in a model of mouse melanoma (Rohner et al., 2015) and in human LN samples (Burns and DePaola, 2005; Kawai et al., 2009; Rebhun et al., 2010). With respect to the effects of disease and inflammation on lymphatic flow rates, a consensus has yet to be reached, with both increases and decreases reported in the context of cancer, inflammation, and other diseases such as lymphedema and obesity (Fujiwara et al., 2014; Harrell et al., 2007; Moore and Bertram, 2018). The concerted effects of these biophysical (structural, flow) and biochemical (adhesion molecule expression) changes on cell adhesion in the context of lymph flow through the LN SCS, however, have yet to be explored.

Altered Shear Stress Profiles Are Predicted within the Remodeled LN SCS

In order to analyze the effects of LN biophysical remodeling (Figure 2A) on fluid flow profiles through the LN SCS (Das et al., 2013; Hampton and Chtanova, 2019; Jakubzick et al., 2013; Leirião et al., 2012), lymph fluid that disperses radially after reaching a planar LN capsule was modeled (Figure 2B) (Das et al., 2013; Hampton and Chtanova, 2019; Jakubzick et al., 2013; Leirião et al., 2012). First, the solution to this fluid velocity profile predicts a WSS (τ in the below equation) profile that decays with radial position roughly an order of magnitude along the length of the afferent-proximal LN SCS (5 versus 0.5 mm), approximated based on reported sizes of human (Dalal et al., 2006) and murine (Zhang et al., 2013) LNs, respectively (Figure 2C and Equation 1).

$$\tau = \frac{3\mu Q}{\pi h^2 r} \qquad \text{(Equation 1)}$$

We note that this highly simplistic approximation neglects several unique attributes of LN flows, though with reasonable justification for a first-order model. First, lymphatic flows are pulsatile in nature but would be expected to be governed by Poiseuille flow, given rates of lymphatic contraction, kinematic viscosity of lymph, and vessel/sinus sizes. Similarly, primary lymphatic valves (Moore and Bertram, 2018; Scallan et al., 2016) may result in lymph propulsion, but their effects on LN flow fields have yet to be well described. As lymph is filtered into the LN parenchyma, the total volumetric flow rate through the SCS would also be expected to diminish along the SCS path, though only to small extents given that it is estimated that ~90% of lymph is directed around the LN periphery through the SCS and medullary sinus (Jafarnejad et al., 2015). Lastly, afferent lymphatics do not necessarily enter LNs orthogonally relative to the capsule, and thus flow at the SCS entrance may be subtly altered to direct lymph into the SCS in a radially non-uniform manner.

Based on this radial flow model approximation, the magnitude of shear stresses experienced by cells lining the sinus wall would be highly sensitive to changes in sinus height (h) and volumetric flow rate (Q), though to a lesser extent for the latter. The magnitude of the peak WSS within the SCS is also a function of lymphatic vessel diameter (LVD), with the peak value decreasing with increasing diameter. Thus, when considering the reported geometries of LNs from human and mouse (Table 1), a wide range of potential WSS values is predicted to be experienced at the LN SCS floor (Figures 2D–2G), though, notably, the order of magnitude is similar between species. Over the range of reported values for Q, maximum to minimum WSS levels range from 0.8–4.0 to 0.2–0.8 dyn/cm^2 (Figures 2D) and 0.6–10 to 0.07–0.7 dyn/cm^2 (Figure 2E), for human and mouse, respectively. Holding Q constant and over the range of SCS h values reported for quiescent LNs (orange), maximum to minimum WSS levels range from 0.4–2.0 to 0.08–0.2 dyn/cm^2 (Figures 2F) and 0.8–10 to 0.07–1 dyn/cm^2 (Figure 2G), for human and mouse, respectively. SCS h values reported for inflamed LNs decrease these WSS levels overall (purple, Figure 2G).

A COMSOL model was also employed to assess the influence of more complex LN geometries on predicted distributions of WSS and cell trajectories in flow (Figure H-I). When assuming an identical geometry,

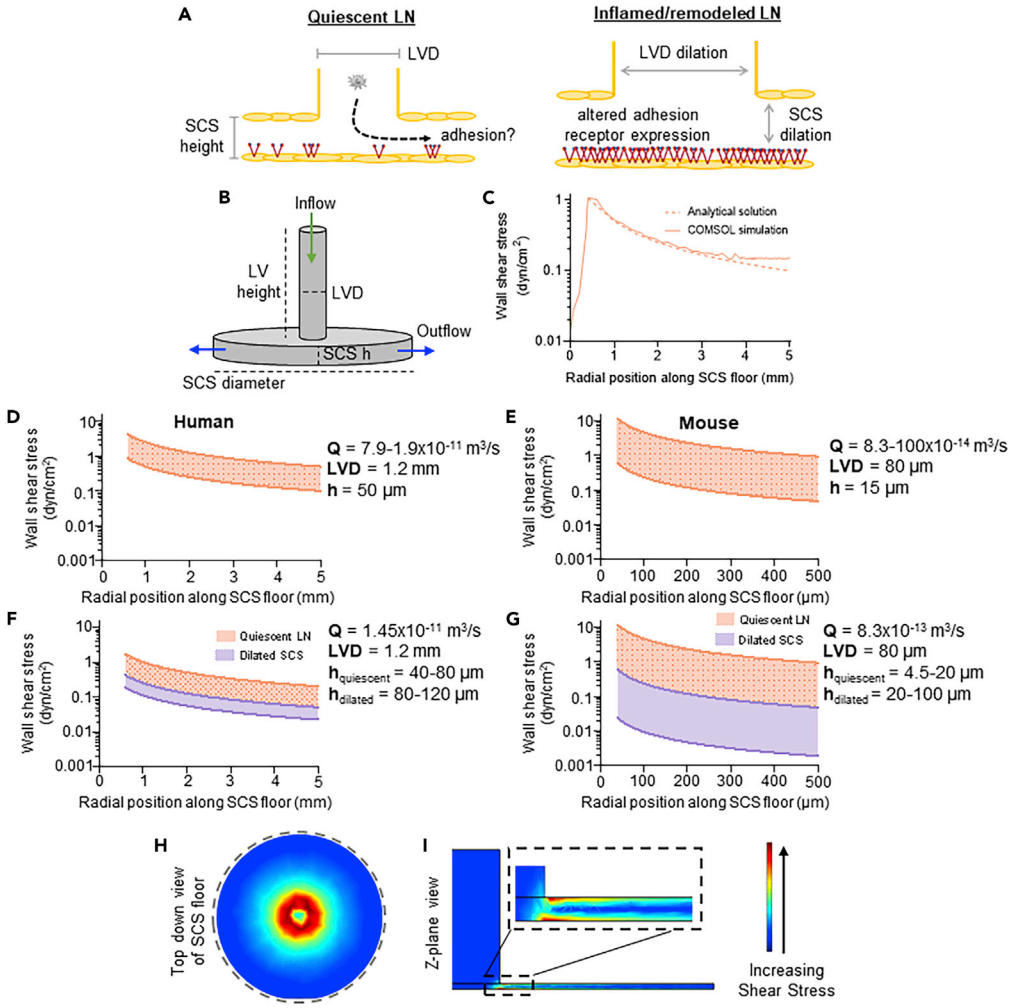

Figure 2. Lymph Fluid Flow Profiles Were Estimated in Quiescent and Remodeled LNs

To model the affect of lymphatic remodeling or inflammation on the ability of a circulating cell to adhere to SCS-lining cells (A), a simplified geometric model of an afferent lymphatic vessel leading into the LN SCS (B) was imported into COMSOL to perform fluid flow simulations quantifying the wall shear stress (WSS) profile along the SCS floor (solid line) (C). This COMSOL-generated WSS estimation was in close agreement to the analytical solution for WSS profiles in a radial flow chamber (dashed line).

(D–G) The analytically calculated ranges of WSS levels for (D, F) human or (E, G) mouse LNs based on maximum and minimum literature cited parameters (Table 1) for (D, E) volumetric flow rate or (F, G) SCS height.

(H and I) COMSOL shear stress simulation plots along the (H) floor of the subcapsular sinus or (I) Z-plane of the radial flow chamber LN model.

this model showed close approximation to the analytical solution (Figure 2C). Within this framework, particle trajectory in flow simulations suggest that alterations in LN geometries minimally influence the likelihood of cells being in contact with the inferior SCS floor upon entry into the LN SCS region (Figure S1). LN curvature was also found to negligibly influence WSS profiles under most physiologically relevant geometric confirmations based on measured LN aspect ratios that were tested (Figure S2A).

Engineered LN Sinus-On-A-Chip Adhesion Microfluidic System

We engineered a LN sinus-on-a-chip parallel plate adhesion flow chamber (Figure 3A) that can be configured to mimic the hydrodynamic SCS microenvironment of a quiescent or remodeled LN, and, specifically here, the dissipating WSS flow fields predicted based on reported lymphatic flow rates and geometric properties of human and mouse LNs. The device, which is easy and rapid to fabricate, is constructed

Reference Parameters	Human			Mouse		
	LVD (mm)	SCS h (μm)	Lymphatic Transit Rate (cm/min)	LVD (μm)	SCS h (μm)	Volumetric Flow Rate (μL/hr)
Quiescent	0.2–21 1–22 0.7–.33	40–804	0.90–4.235	50–806 907	13.98 15–209 4.5–1,310	0.3–4.011
Inflamed/remodeled	1–212 1–313	80–12,014	0.95–5.765	120–30,014	20–5,716 50–10,017	NA

Table 1. Reference Ranges of Mouse and Human LN Parameters

from a sheet of polydimethylsiloxane and a polystyrene tissue culture plate between which is a 125 μm adhesive gasket. High-speed videomicroscopy enabled visualization of cell adhesion of an infused cell pulse along the length of the divergent portion of the channel (Figure 3B), which was functionalized with adhesion receptors (Birmingham et al., 2019; 2020; Edwards et al., 2018; Oh et al., 2015) to recapitulate their expression on the lymphatic endothelial cell-lined SCS floor (Figure 3C). The channel was also designed with a 10-cm long unfunctionalized portion (Figures 3A and 3B) sufficient in length to allow perfused cells to be uniformly in contact with the substrate, enabling all cells used in this work to settle to the channel bottom prior to reaching the functionalized section (Birmingham et al., 2019). This design choice was made to ensure all perfused cells have uniform contact with the functionalized surface and thus the measured extents of adhesion are comparable between perfusion conditions. In addition, cells entering LNs are expected to immediately be in contact with the SCS floor upon arrival from the afferent vessel based on particle trajectory analyses using an idealized planar SCS geometry (Figure S1). Simulated WSS profiles were then recapitulated within this perfusion system to close approximation (Figure S2B) through two means: (1) the use of a 4-cm long divergent channel region functionalized with adhesion molecules that increases linearly in width from 0.2 cm to 1.2 cm (Figures 3D) and (2) by simply varying the volumetric flow rate of fluid perfusion through the system using the inline syringe pump.

Consensus Q, LVD, and h values were selected (Figure 3E) based on published literature (Table S1) (Das et al., 2013; Harrell et al., 2007; Hinson et al., 2017; Hoshida et al., 2006; Jafarnejad et al., 2015; Karnezis et al., 2012; Nakayama et al., 1999; Ohtani and Ohtani, 2008; Singh and Choi, 2019; Turner and Mabbott, 2017), to recapitulate approximate WSS levels predicted to be experienced within quiescent versus inflamed LNs (Figure 2F) in the LN sinus-on-a-chip microfluidic system (Figure 2F and Table S2). The influence of increased LVD and h were individually assessed, given that the necessary co-occurrence of LVD and SCS dilation has yet to be definitively established (Das et al., 2013; Elmore, 2006; Kawai et al., 2009; Ozasa et al., 2012; Sweety and Narayankar, 2019). Under these conditions, Q was also left unchanged, an approximation deemed reasonable given that its magnitudes are less well characterized (Dixon et al., 2006; Jafarnejad et al., 2015).

LN SCS Flow Microenvironment Regulates Robust Adhesion by Cancerous and Monocytic Cells

The adhesive behaviors of human colon and pancreatic carcinoma cell lines LS174T and PANC-1 that form lymphatic metastases in xenograft tumor models (Delitto et al., 2017; Emir et al., 2007) were assessed. This allowed for elucidation of the effects of LN-remodeling-mediated changes in the dissipating WSS range within the LN SCS on key aspects of carcinoma cell biology. Briefly, cells were perfused individually at varying flow rates through the microfluidic system that was functionalized within the divergent portion with various combinations of lymphatic-endothelium-expressed adhesion receptors. Specifically, four different functionalization schemes were used: 2.5 μg/mL E-selectin alone (1) or in combination with 2.5 μg/mL ICAM (2), 2.5 μg/mL VCAM (3), or 10 μg/mL VCAM (4). These molecules were chosen given their widely appreciated roles in mediating cell adhesion in fluid flow (Edwards et al., 2017; Kawai et al., 2009; Schlesinger and Bendas, 2015), expression by SCS lining cells (Berendam et al., 2019), reported changes in LN expression in inflammation (Burns and DePaola, 2005; Kawai et al., 2009; Rebhun et al., 2010), and potential role in LN metastasis (Yan et al., 2014). These specific concentrations of adhesive ligands were selected based on extensive prior characterization by our group demonstrating 2.5 μg/mL Fc-specific anti-IgG to be a minimum concentration that consistently provides uniform functionalization of the microfluidic surface.

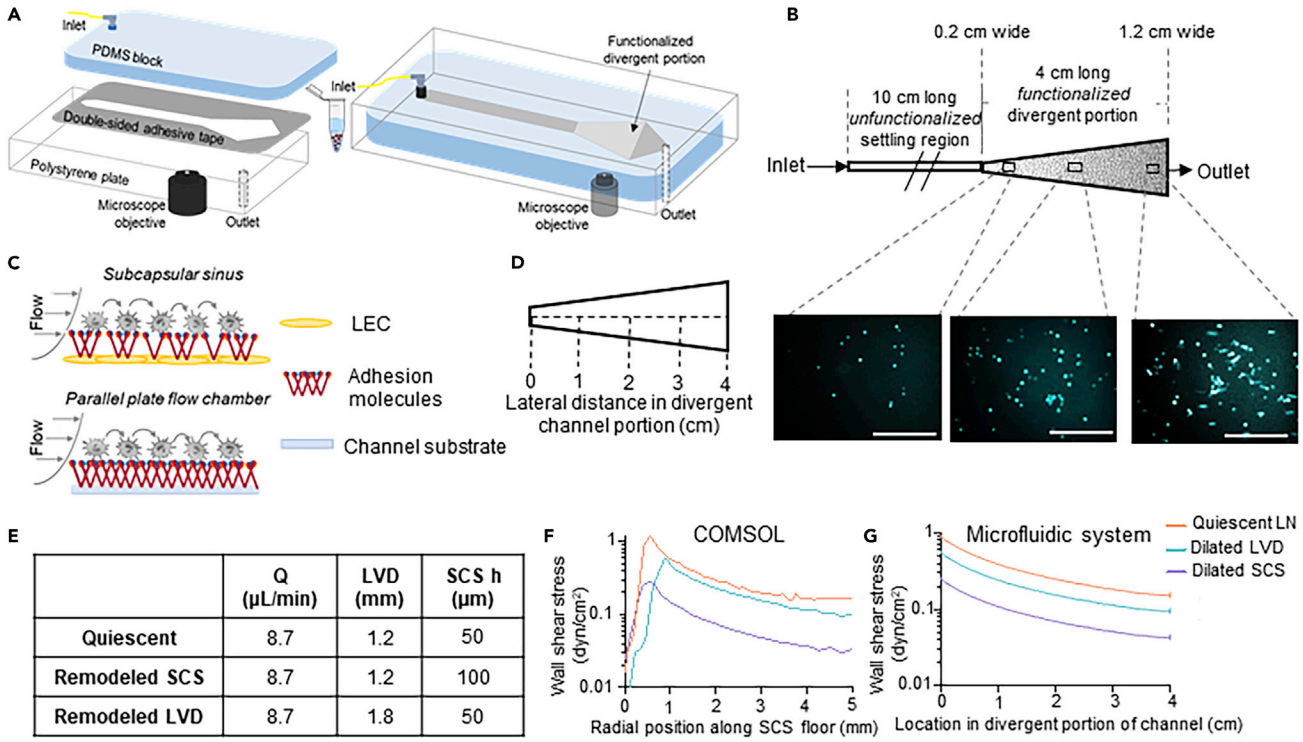

	Q (μL/min)	LVD (mm)	SCS h (μm)
Quiescent	8.7	1.2	50
Remodeled SCS	8.7	1.2	100
Remodeled LVD	8.7	1.8	50

Figure 3. Divergent Channel Perfusion System Interrogates Effects of LN SCS-Mimicking Flow on Cell Adhesion *In Vitro*

Motivated by dissipating WSS profiles analytically predicted using COMSOL models of LNs, (A) a SCS microenvironment-mimicking, divergent parallel-plate microfluidic perfusion was designed and fabricated. (B and C) The channel was designed with an unfunctionalized settling portion connected to an adhesion-molecule-functionalized, divergent portion that has a linearly increasing flow channel width. Cell adhesion at various locations along the channel center line (D) was visualized by phase contrast or fluorescent imaging using an integrated high speed videomicroscopy system. Scale bar, 200 μm. The divergent shape was designed, and perfusion parameters were selected (E) to recapitulate the WSS profiles of quiescent and remodeled/inflamed LNs predicted from COMSOL simulations (F) that show close agreement in magnitude but not channel position, given the desire to minimize WSS changes over each imaging FOV (G).

Furthermore, we have previously reported that this level of E-selectin used for immobilization is capable of mediating extensive, but non-saturating, levels of cell adhesion in flow (Edwards et al., 2017) and that changes in ICAM concentration has no effect on the extent of cell adhesion in flow (Edwards and Thomas, 2017). Likewise, there is a dynamic range of VCAM expression by lymphatic endothelial cells due to inflammatory mediators (Lund et al., 2016b; Vigl et al., 2011). Cell adhesion was quantified within the perfusion system by counting the number of interacting cells and quantification of the average rolling velocity of the interacting cells at 0.5 cm increments along the center of the functionalized, divergent portion of the flow channel (left column, Figures S3–S9) over 30 s intervals. As each measurement location corresponds to a different local WSS level (Table S1), comparisons between the extent of adhesion and rolling velocity at similar channel positions and WSS levels were also made (Figures 4, 5, 6, 7, and S3–S9).

Adhesion by LS174T colon carcinoma cells, which are well studied for their adhesive properties within flow fields (Birmingham et al., 2019; 2020; Erin E. Edwards et al., 2018; Oh et al., 2015) and express a variety of adhesion ligands for selectins (Dallas et al., 2012; Hanley et al., 2006) and other CAMs (Paschos et al., 2010), were evaluated (Birmingham et al., 2019, 2020; Dallas et al., 2012; Edwards et al., 2017, 2018; Hanley et al., 2006; Thomas et al., 2008). Consistent with prior reports (Fujisaki et al., 1999), LS174T cells did not adhere in flow to ICAM or VCAM (Figures 4D, 4H, and 4L) alone under any tested configuration of flow but interacted extensively with E-selectin (Figures 4A and 4C) at rolling velocities unchanged by flow condition (Figure 4B). Perfusion in flow experiment configurations with lower WSS ranges, modeling dilation of the LVD and SCS, appeared to decrease the WSS level at which maximal adhesion occurred (Figure 4A). However, when considering channel position, the extent of adhesion by LS174T cells was only changed for the dilated SCS relative to the quiescent LN model (Figure 4C). Thus, the initial increase in adhesion upon initial entry into the functionalized channel without changes in velocities of rolling cells skew the WSS dependency of

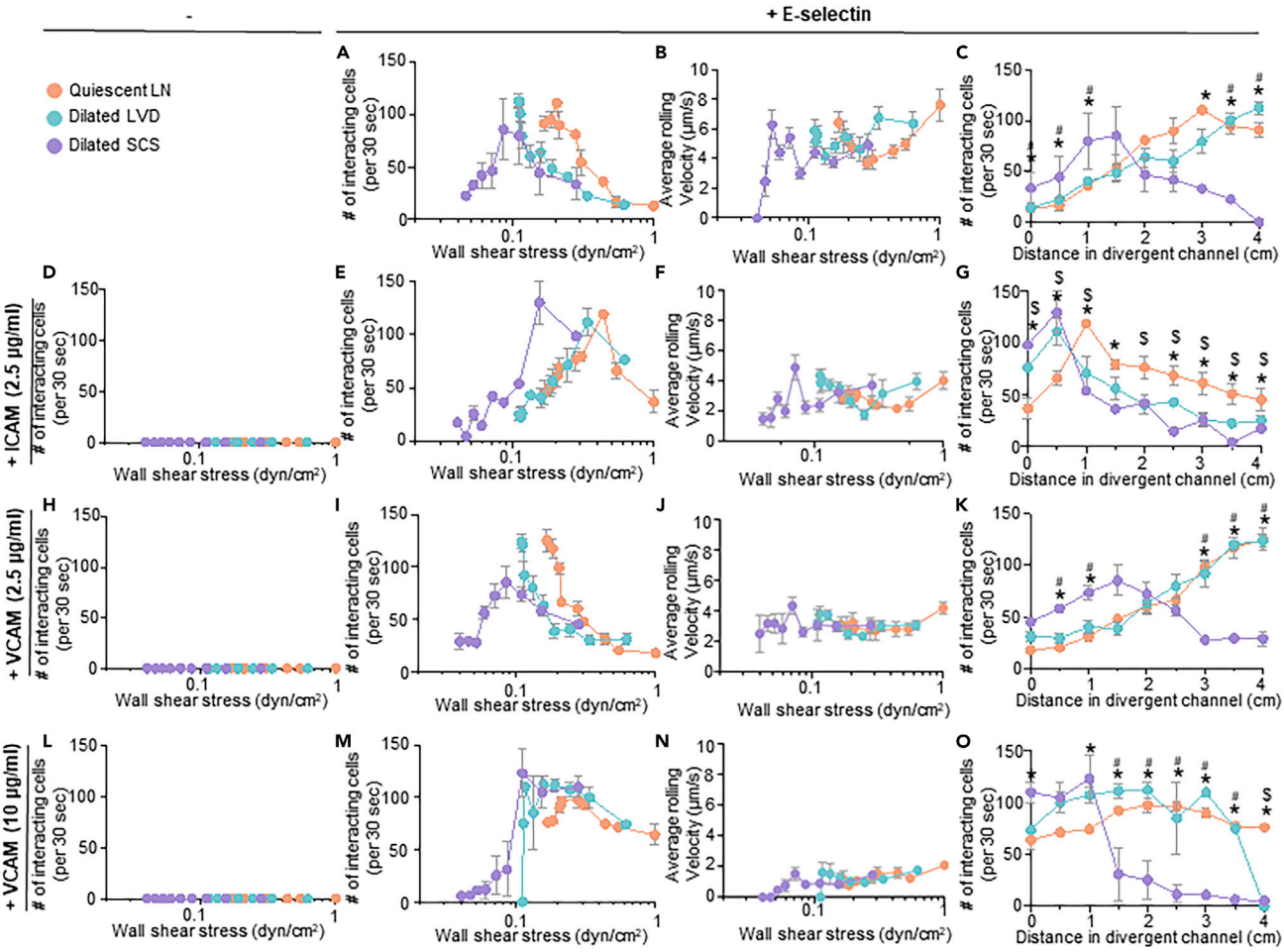

Figure 4. The WSS Dependency of LS174T Colon Carcinoma Cell Adhesion in LN SCS-Mimicking Flow Fields and Microenvironments Is Modified by Altered Flow Profiles Predicted to Result from LVD and SCS Dilation

The number and average rolling velocity of LS174T cells adhering in flow in divergent channels functionalized with (A–C) 2.5 μg/mL E-selectin alone, (D) 2.5 μg/mL ICAM alone, (E–G) 2.5 μg/mL E-selectin + 2.5 μg/mL ICAM, (H) 2.5 μg/mL VCAM alone, (I–K) 2.5 μg/mL E-selectin + 2.5 μg/mL VCAM, (L) 10 μg/mL VCAM, or (M–O) 2.5 μg/mL E-selectin + 10 μg/mL VCAM. Data are represented as mean ± SEM. *, #, and $ indicate significance ($p<0.05$) by two-way ANOVA with Tukey's post-hoc test, between quiescent LN and dilated SCS, dilated LVD and dilated SCS, and quiescent LN and dilated LVD, respectively.

LS174T cell adhesion to E-selectin in the dilated SCS flow model. Similar effects were also seen for the dilated SCS flow model with respect to LS174T cell adhesion to ICAM and VCAM co-presented with E-selectin (Figures 4E–4G, 4I–4K, and 4M–4O). However, adhesion under perfusion conditions modeling dilated LVD flow closely mirrored those seen for quiescent LN flow models, save for E-selectin co-presented with ICAM wherein adhesion was increased at more channel inlet-proximal positions (Figure 4C), and resulted in identical dependencies of adhesion on WSS (Figure 4A). Under flow conditions modeling quiescent LNs, co-presentation of ICAM increased the overall extent of adhesion at WSS levels >0.4 dyn/cm^2 (Figure 5A) and additionally decreased rolling velocities at WSS levels <0.2 dyn/cm^2 (Figure 5B) relative to adhesion on E-selectin alone. Similar effects of ICAM co-presentation on the extent and velocity of rolling cell adhesion in flow were also seen in dilated LVD and SCS perfusion models, with subtle changes in the WSS levels relative to the quiescent LN model (Figures 5A and 5B). Co-presentation of VCAM at a concentration of 2.5 μg/mL decreased rolling velocities compared with adhesion to E-selectin alone to similar extents as ICAM under all tested flow conditions (Figure 5B) despite having no effect on the overall extent of adhesion (Figure 5A). Effects on rolling velocity magnitude compared with E-selectin were more substantial for the higher (10 μg/mL) VCAM concentration (Figure 5B) and, in contrast to the lower concentration tested, resulted in higher extents of adhesion under all tested flow conditions (Figure 5A). Co-presentation of ICAM and VCAM changed the location of maximal cell adhesion to more inlet-proximal channel

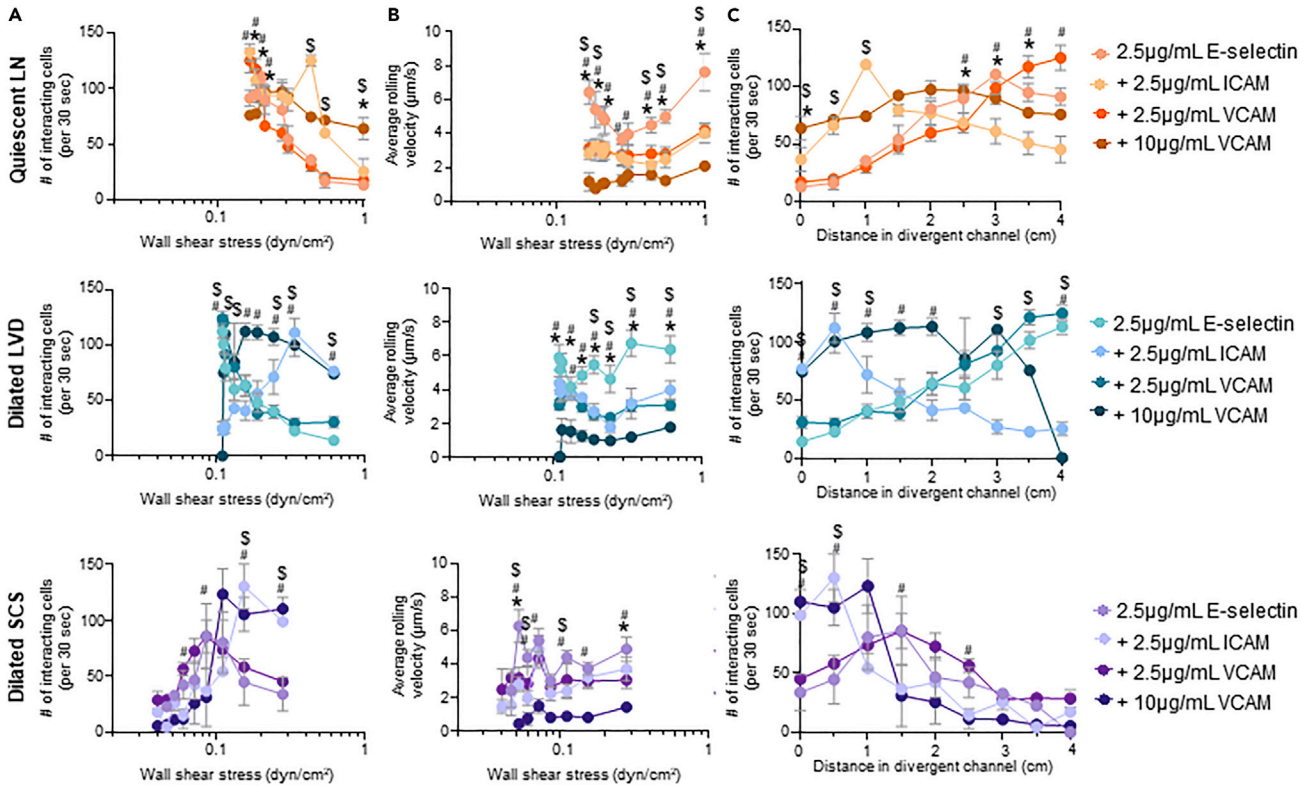

Figure 5. Co-presentation of Adhesion Molecules Alters the WSS Dependency of LS174T Cell Adhesion in Flow

The number (A and C) and average rolling velocity (B) of LS174T cells adhering to E-selectin alone or when co-presented with ICAM or VCAM in flow regimes modeled after a quiescent LN (top row), LN with a dilated LVD (middle row), or LN with a dilated SCS (bottom row). Data are represented as mean ± SEM. *, #, and $ indicate significance ($p<0.05$) by two-way ANOVA with Tukey's post-hoc test, between E-selectin and E-selectin + 2.5 μg/mL VCAM, E-selectin and E-selectin + 10μg/mL VCAM, and E-selectin and E-selectin + 2.5μg/mL ICAM, respectively.

positions relative to that resulting from E-selectin alone, save in the context of co-presentation of low (2.5 μg/mL) concentrations of VCAM (Figure 5C). These results demonstrate the flow microenvironment experienced by LS174T cells critically regulates their adhesion extent that is further influenced by the context of adhesive molecule presentation.

Adhesion of PANC-1 pancreatic cancer cells, which have been shown *in vivo* to form metastatic tumors and also express numerous functional selectin, ICAM, and VCAM ligands, including sialyl Lewis x, lymphocyte-function-associated antigen 1, and very late antigen 4 (Fan et al., 2015; Kate et al., 2006), respectively, was next explored. Unlike LS174T cells, these cells adhered minimally to E-selectin (Figure S3A) at rolling velocities unchanged by flow condition with respect to WSS dependency (Figure S3B). They also exhibited adhesion in flow to ICAM and VCAM only when co-presented with E-selectin (Figures S3A, S3D, S3H, and S3L), with rolling velocity magnitudes that were independent of perfusion condition (Figures S3F, S3J, and S3N). Perfusion under flow conditions modeling dilated LVD had no effect relative to quiescent LN flow models on the WSS dependency of PANC-1 cell adhesion in flow under any tested functionalization scheme (Figures S3A, S3E, S3I, and S3M). In the context of E-selectin co-presentation with ICAM and high (10 μg/mL), but not low (2.5 μg/mL), VCAM, however, flow modeling a dilated SCS increased the extent of adhesion upon cell entry into the functionalized channel portion compared with that observed in flow modeling quiescent LNs (Figure S3C), mirroring LS174T cell adhesion under all tested functionalization schemes (Figures 4C, 4G, 4K, and 4O). In the context of ICAM but not VCAM (10 μg/mL) co-presentation, the dependency of the extent of adhesion on WSS, however, was sustained. In flow regimes modeling quiescent LNs and dilated LVD, co-presentation of both ICAM and 10 μg/mL VCAM increased the extent of PANC-1 cell adhesion relative to E-selectin alone (Figure S4A), despite no effects on rolling velocity magnitude (Figure S4B). Adhesion by PANC-1 cells was also increased by co-presentation of ICAM and VCAM at either tested concentration in modeled dilated SCS flow (Figure S4A). The net effect of ICAM and VCAM

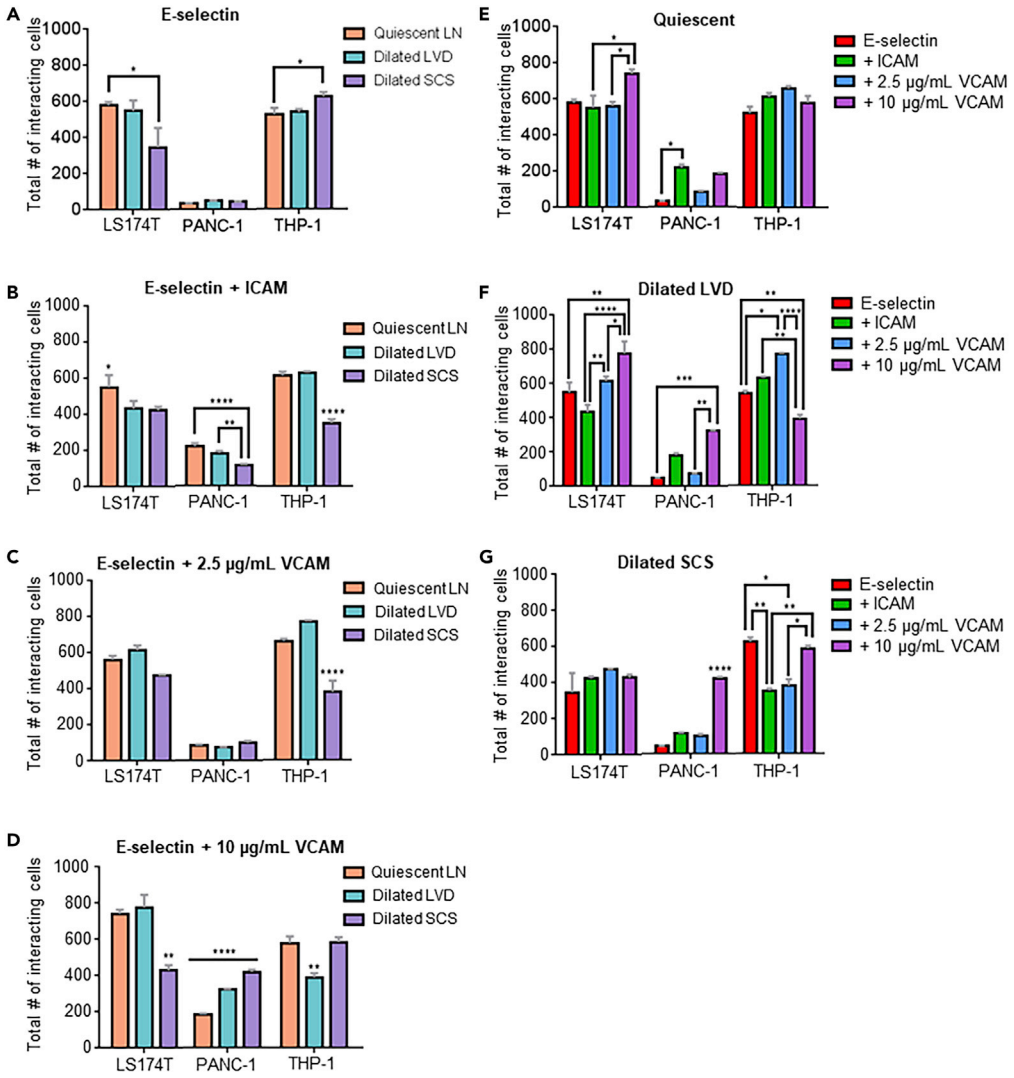

Figure 6. Flow Microenvironment and Adhesive Molecule Presentation Impact Cumulative Extent of Cell Adhesion along Channel Length

(A–D) Influence of LN SCS-mimicking flow regime during flow across E-selectin (A), E-selectin + ICAM (B), E-selectin + 2.5 ug/mL VCAM (C), and E-selectin + 10 ug/mL (D).

(E–G) Influence of adhesive molecule presentation in microfluidics modeling the quiescent LN (E), dilated LVD (F), and dilated SCS (G). Data are represented as mean ± SEM. * ($p<0.05$), ** ($p<0.01$), *** ($p<0.001$), and **** ($p<0.0001$) indicate significance by one-way ANOVA with Tukey's post-hoc test.

co-presentation was an overall increase in adhesion extent relative to E-selectin presentation alone and not a change in location of maximal cell adhesion within the channel (Figure S4C). These results suggest the extent of PANC-1 adhesion in flow to be critically regulated by presentation of adhesive molecules and flow microenvironment when adhesion is robust.

Monocytes migrate to LNs from peripheral tissues via the afferent lymphatic vessel and into the LN SCS during states of inflammation and disease (Harmsen et al., 1985; Lund et al., 2016b; Maletto et al., 2006). We therefore explored adhesion by monocytic cell line THP-1 in the context of LN SCS-mimicking flow fields. THP-1 cells did not adhere in flow to ICAM or VCAM alone under any tested configuration of flow (Figures S5D, S5H, and S5L), consistent with previous reports (Edwards and Thomas, 2017). They did, however, interact extensively with E-selectin (Figure S5A) at velocities unchanged by flow condition (Figure S5B). In the context of altered flow regimes, the dilated SCS experimental flow model appeared to diminish the WSS level of maximal THP-1 cell adhesion to E-selectin (Figure S5A), an effect associated

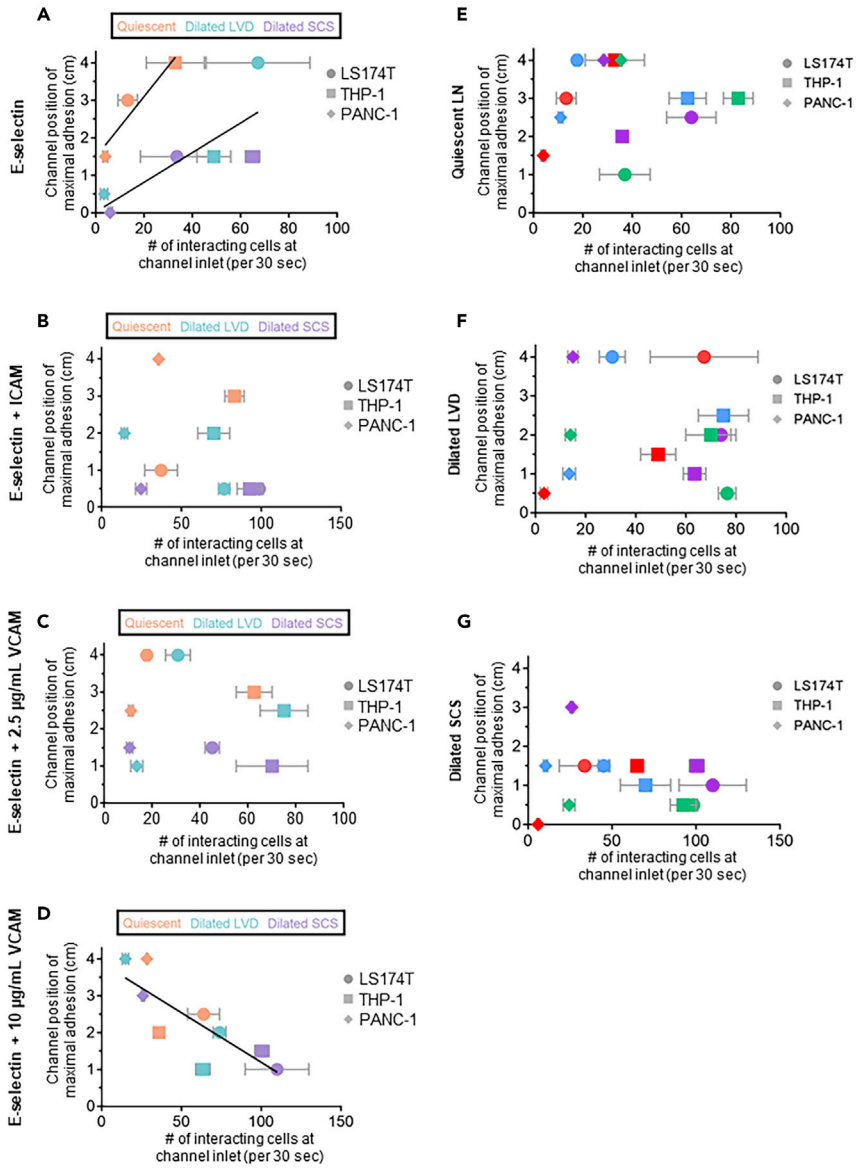

Figure 7. Flow Microenvironment and Adhesive Molecule Presentation Impact Relationships between Initial Adhesion Extent and Channel Position of Maximal Cell Adhesion

(A–D) Influence of LN SCS-mimicking flow regime during flow across E-selectin (A), E-selectin + ICAM (B), E-selectin + 2.5 ug/mL VCAM (C), and E-selectin + 10 ug/mL VCAM (D)Lines represent statistically non-zero slopes ($p<0.05$) of linear regressions of (A) quiescent series (left fit) or pooled data for dilated LVD and SCS series (right fit) and (D) all series pooled. (E–G) Influence of adhesive molecule presentation in models of the quiescent LN (E), dilated LVD (F), and dilated SCS (G). Data are presented as mean ± SEM.

with higher extents of adhesion at channel locations more proximal to the inlet (Figure S5C). Similar trends were observed when cells were perfused over E-selectin co-presented with 10 µg/mL VCAM, where adhesion (in this case firm adhesion, as measured rolling velocities were 0 um/s) was sustained at lower levels of WSS (Figures S5M and S5N). Under these functionalization conditions, high levels of adhesion by THP-1 cells in flow was restricted to inlet-proximal channel positions (Figure S5O). Co-presentation of E-selectin with VCAM at lower concentrations (2.5 µg/mL) similarly restricted high levels of adhesion to inlet-proximal channel locations, albeit in the context of dilated SCS flow regimes only (Figure S5K), and had no effect on the WSS dependency of adhesion extent (Figure S5I). The WSS dependency of adhesion by THP-1 cells in the context of E-selectin co-presentation with ICAM was similarly unchanged (or nearly so, given the subtle

change in drop of extent adhesion between 0.1 and 0.2 dyn/cm^2) by perfusion condition (Figure S5E). The net effect was maximal adhesion by THP-1 cells to be more restricted to the start of functionalized channel in the context of dilated LVD and SCS compared with quiescent LN flow models (Figure S5G). Under flow conditions modeling quiescent LNs, co-presentation of ICAM increased the overall extent of THP-1 cell adhesion at WSS levels >0.3 dyn/cm^2 (Figure S6A) and decreased rolling velocities additionally at WSS levels >0.6 dyn/cm^2 (Figure S6B) relative to adhesion on E-selectin alone. Similar effects of ICAM co-presentation with E-selectin on the extent and velocity of rolling cell adhesion in flow were also seen in dilated SCS but not LVD perfusion models at WSS levels ~0.15 dyn/cm^2 and lower (Figures S6A and S6B). E-selectin co-presentation with VCAM also increased the extent, but not velocity of rolling adhesion in all tested flow models, although only for the highest functionalization concentration in the context of quiescent LN and dilated LVD flow models (Figures S6A and S6B). As a result, ICAM and VCAM co-presentation restricted the region of maximal cell adhesion to more inlet-proximal channel positions relative to that resulting from E-selectin alone, save in the contexts of low VCAM or ICAM co-presentation in flows modeling quiescent LNs and dilated LVD, respectively (Figure S6C). These results demonstrate that, as LS174T cells, the flow microenvironment experienced by THP-1 cells critically regulates their adhesion extent that is further influenced by the context of presented adhesive molecules.

Extent and Trajectory of Cell Adhesion Within Perfusion Channel Are Interdependently Regulated by Dissipating WSS Regime, Adhesive Ligand Presentation, and Initial Adhesive Interactions at Channel Inlet

Although WSS dependencies of cell adhesion were found to be only subtly regulated by flow regime, trajectories of cell adhesion within the perfusion channel varied widely. The cumulative effects of both flow microenvironment and adhesive ligand presentation on overall adhesion by cells in SCS-mimicking flow fields were made apparent by analysis of total adhesion over the channel length (e.g. the summation of total adherent cells at each analyzed FOV). Flow fields modeling dilated SCS resulted in adhesion to E-selectin alone to be increased versus decreased for LS174T and THP-1 cells, respectively (Figure 6A). When co-presented with ICAM, E-selectin-mediated adhesion by metastatic cells was decreased in flow fields modeling the influence of dilated SCS compared with quiescent LNs (Figure 6B). Adhesion by metastatic cells was unchanged in dilated SCS-mimicking flows when perfused over E-selectin co-presented with low (2.5 μg/mL) VCAM levels (Figure 6C). When co-presented with high levels of VCAM (10 μg/mL), however, flows modeling the dilated LN SCS resulted in lower versus higher adhesion by LS174T and PANC-1 cells, respectively, compared with that seen in flow fields modeling quiescent LNs (Figure 6D). E-selectin-mediated adhesion by THP-1 cells in flow was similarly regulated by flow microenvironment in a complex manner. Flow microenvironments modeling the dilated SCS resulted in increased adhesion to E-selectin alone and diminished adhesion when E-selectin was co-presented with ICAM or 2.5 μg/mL VCAM (Figures 6A–6C). Flow fields modeling dilated LVD had minimal effects, diminishing LS174T cell adhesion to E-selectin co-presented with ICAM (Figure 6B) and decreasing THP-1 cell adhesion to E-selectin co-presented with 10 μg/mL VCAM (Figure 6D).

When considering a constant flow microenvironment, effects of adhesive molecule presentation on the total extent of adhesion along the channel length were also apparent. Although adhesion by THP-1 cells remained unaffected, increased adhesion by LS174T cells was observed with 10 μg/mL VCAM co-presentation and by PANC-1 cells with ICAM co-presentation (Figure 6E). Under conditions mimicking dilated LVD, 10 μg/mL VCAM co-presentation with E-selectin increased adhesion by metastatic cancer cells and decreased THP-1 cell adhesion (Figure 6F). Co-presentation of E-selectin with 2.5 μg/mL VCAM also increased adhesion by THP-1 cells (Figure 6F). Co-presentation with ICAM, however, did not affect adhesion by any tested cell type compared with E-selectin alone (Figure 6F). In flow fields modeling a dilated SCS, adhesion by LS174T cells remained unchanged (Figure 6G). However, adhesion by PANC-1 cells was increased by co-presentation with 10 μg/mL VCAM and decreased for THP-1 cells when either ICAM or 2.5 μg/mL VCAM was co-presented (Figure 6G). Together, these results demonstrate the complex interplay of both flow microenvironment and adhesive molecule presentation in the regulation of adhesion extent by both metastatic cancer and monocytic cells in SCS-mimicking flow fields.

The capacity for cells to mediate adhesion in flow is influenced by both secondary tethering as well as length of contact with an adhesive substrate during transit in the flow direction (Edwards and Thomas, 2017). As such, the influence of flow microenvironment on the extent of initial adhesion at the channel inlet (0 cm into divergent channel) versus the channel position at which cell adhesion was maximal was

tabulated. When perfused over E-selectin alone, adhesion by cells in flow fields mimicking quiescent LNs became maximal at channel positions farther in the flow direction at correspondingly lower extents of initial adhesion when compared with that seen for dilated LVD and SCS flow fields (Figure 7A). Regression analysis revealed significant relationships between channel position and number of interacting cells ($p<0.0001$ when compared with a slope of 0 for both quiescent and inflamed scenarios with r2 values of 0.9023 and 0.6482, respectively), with the quiescent LN flow fields demonstrating higher extents of initial adhesion ($p=0.0215$) (Figure 7A). On the other hand, no discernable relationships between initial adhesion extent and channel position of maximal adhesion were seen for E-selectin when co-presented with either ICAM or 2.5 μg/mL VCAM, with no non-zero slopes found by linear regression ($p = 0.187$ and 0.8141, respectively; Figures 7B and 7C). Under these conditions, however, flow fields modeling dilated SCS did result in maximal adhesion at more inlet proximal positions for all three tested cell types compared with flow fields modeling quiescent LNs (Figures 7B and 7C). In distinct contrast to trends seen for adhesion to E-selectin alone, co-presentation with 10 μg/mL VCAM resulted in maximal E-selectin-mediated cell adhesion occurring at more inlet proximal channel positions when initial adhesion was greater, a trend seen irrespective of flow microenvironment (Figure 7D). Linear regression analysis revealed a non-zero slope ($p<0.0001$) with high correlation (r2=0.6869; Figure 7D), fortifying this conclusion. Under comparable perfusion flow conditions, no relationship between the levels of initial adhesive interactions and channel positions at which maximal adhesion was measured were observed (Figures 7E–7G). These results demonstrate the potential for both flow microenvironment and adhesive molecule presentation to regulate the trajectory of adhesion within the LN SCS microenvironment.

LS174T cell Adhesion in Flow Is Increased by Co-Perfusion with THP-1 Cells

Monocytes have been reported to facilitate adhesive interactions by metastatic cancer cells (León et al., 2007; Lund et al., 2016b; Randolph et al., 1999; Shi and Pamer, 2011). The effects of THP-1 monocytic cells on adhesive interactions by metastatic LS174T colon carcinoma cells in LN SCS-mimicking flow fields and adhesive microenvironments were thus investigated. Specifically, a total of 105 LS174T cells diluted with different amounts of THP-1 cells to LS174T:THP-1 ratios (3:1, 1:1, and 1:3) were perfused over E-selectin functionalized surfaces under quiescent LN or dilated LVD and SCS flow configurations. Under all tested flow conditions, co-perfusion both increased the number of interacting cells (Figure 8A) and decreased the average rolling velocity of interacting cells (Figure 8B). In flow fields modeling quiescent LNs, increased adhesion was seen at WSS levels of >0.4 dyn/cm^2 (although not statistically significant at 1.0 dyn/cm2) versus >0.3 dyn/cm^2 for perfused cell ratios of 1:1 and 1:3, respectively (Figure 8A) and slower rolling velocities at all WSS levels tested for cell ratios of 1:3 and from 0.3–0.5 dyn/cm^2 for cell ratios of 1:1 (Figure 8B). In flow regimes mimicking inflamed LNs, perfused cell ratios of 1:3 increased the extent of adhesion over all tested WSS levels and above ~0.15 dyn/cm^2 for dilated LVD versus SCS, respectfully (Figure 8A) where corresponding decreases in cell velocities were also measured, and in the case of dilated SCS flow extended to 0.04–0.07 dyn/cm^2 WSS levels (Figure 8B). The extent of LS174T adhesion to E-selectin by cells perfused at ratios of 1:1 was also increased over all tested WSS levels in flow modeled after dilated LVD and ~0.1 and 0.2 dyn/cm^2 for dilated SCS flow regimes (Figure 8A). The velocity of rolling adhesion was also generally decreased at these conditions under which the number of interacting cells was generally higher (Figure 8B). A cell perfusion ratio of 3:1 tended to have the smallest overall effect on E-selectin adhesion by LS174T cells, having no influence in quiescent LN flow, and increasing adhesion at WSS levels less than ~0.15 dyn/cm^2 versus ~0.3 dyn/cm^2 in dilated LVD versus SCS flows, respectively (Figure 8A). Magnitudes of rolling adhesion velocities were also decreased at WSS levels >0.115 dyn/cm^2 (save at 0.25 dyn/cm^2) and 0.04–0.07 dyn/cm^2 for dilated LVD versus SCS flow regimes, respectfully (Figure 8B). To verify that increased adhesion did not result strictly from alterations in sterics/cellular collisions, the extent of adhesion by 2x the number of perfused LS174T cells (2x105) was assessed (Figure S7). In all three flow regimes, the extent of adhesion per 105 LS174T cells was equivalent over all WSS levels, in distinct contrast to when diluted to a 1:1 ratio with 105 THP-1 cells to a total perfusion cell count of 2x105 (Figure S7). These findings are strongly suggestive of THP-1 cells modulating LS174T cell adhesivity with E-selectin in a manner that is WSS magnitude- and dissipation rate-dependent.

The influence of co-perfusion with THP-1 cells on LS174T cell adhesion to various configurations of adhesive ligand co-presentation was next investigated. Using a 1:1 ratio of cells (for a total of 2x105 cells perfused and adhesion by 105 fluorescent LS174T cells quantified), adhesion to E-selectin co-presented with ICAM or VCAM under various flow configurations was quantified using fluorescent microscopy. The

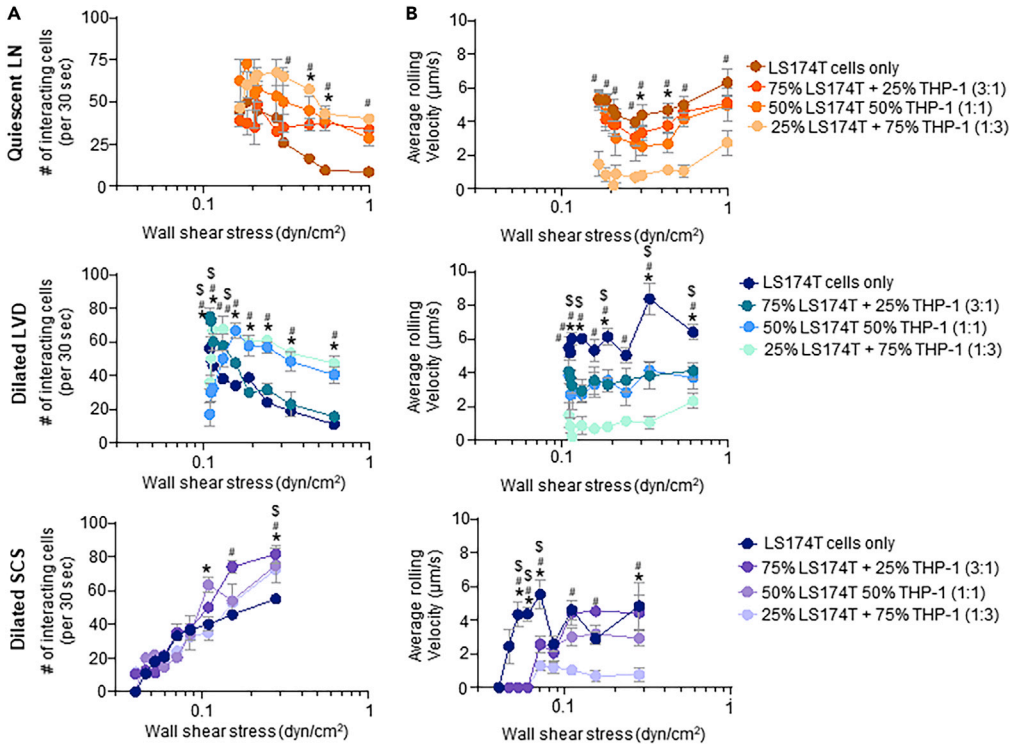

Figure 8. Extent of Adhesion and WSS Dependency of LS174T Cell Adhesion to E-Selectin in Flow Is Regulated by Amount of Co-perfused THP-1 Cells

The number (A) and average rolling velocity (B) of LS174T cells adhering to E-selectin in flow regimes modeled after a quiescent LN (top row), LN with a dilated LVD (middle row), or LN with a dilated SCS (bottom row). Data are presented as mean ± SEM. *, #, and $ indicate significance ($p<0.05$) by two-way ANOVA with Tukey's post-hoc test, between LS174T cells only versus 50% LS174T + 50% THP-1, LS174T versus 75% LS174T + 25% THP-1, and LS174T versus 25% LS174T + 75% THP-1, respectively.

extent and velocity of rolling adhesion by LS174T cells in the context of E-selectin co-presentation with ICAM was generally increased (Figure 9A) and decreased (Figure 9B), respectfully, when co-perfused with THP-1 cells for all tested flow models. THP-1 cell co-perfusion generally had a weaker effect on the extent of adhesion by LS174T cells to E-selectin co-presented with VCAM. When functionalized with low (2.5 μg/mL) levels of VCAM, co-perfusion both increased and decreased the extent of adhesion in the context of quiescent LN flow configurations at high versus low WSS levels, respectively, and increased somewhat the extent of adhesion at WSS levels >0.12 dyn/cm^2 in dilated SCS flow (Figure 9C). More substantial influences were seen for adhesion to E-selectin when co-presented with 2.5 μg/mL VCAM under dilated LVD flow, where adhesion extents were increased when LS174T cells were co-perfused with THP-1 cells (Figure 9C), whereas rolling velocities were generally unaffected (Figure 9D). Co-perfusion with THP-1 cells only very modestly increased adhesion (Figure 9E) and diminished the velocities (Figure 9F) of LS174T cell adhesion at high (10 μg/mL) VCAM co-functionalization levels. This suggests that co-perfusion with THP-1 cells generally enhances the adhesive propensity of LS174T cells most substantially in the context of adhesion to E-selectin alone or when co-presented with ICAM in a manner regulated by flow regime.

DISCUSSION

Engineered microfluidic systems represent unique *in vitro* tools capable of uncoupling the influences of adhesive molecule expression levels and/or spatial patterns, vessel size, and flow rates that change *in vivo* as a result of vascular remodeling in pathological states to orchestrate local cell recruitment/homing to sites of inflammation on the regulation of cell adhesion in flow. For example, previous work from our group explored the influence of adhesive molecule presentation length in the translational flow direction on

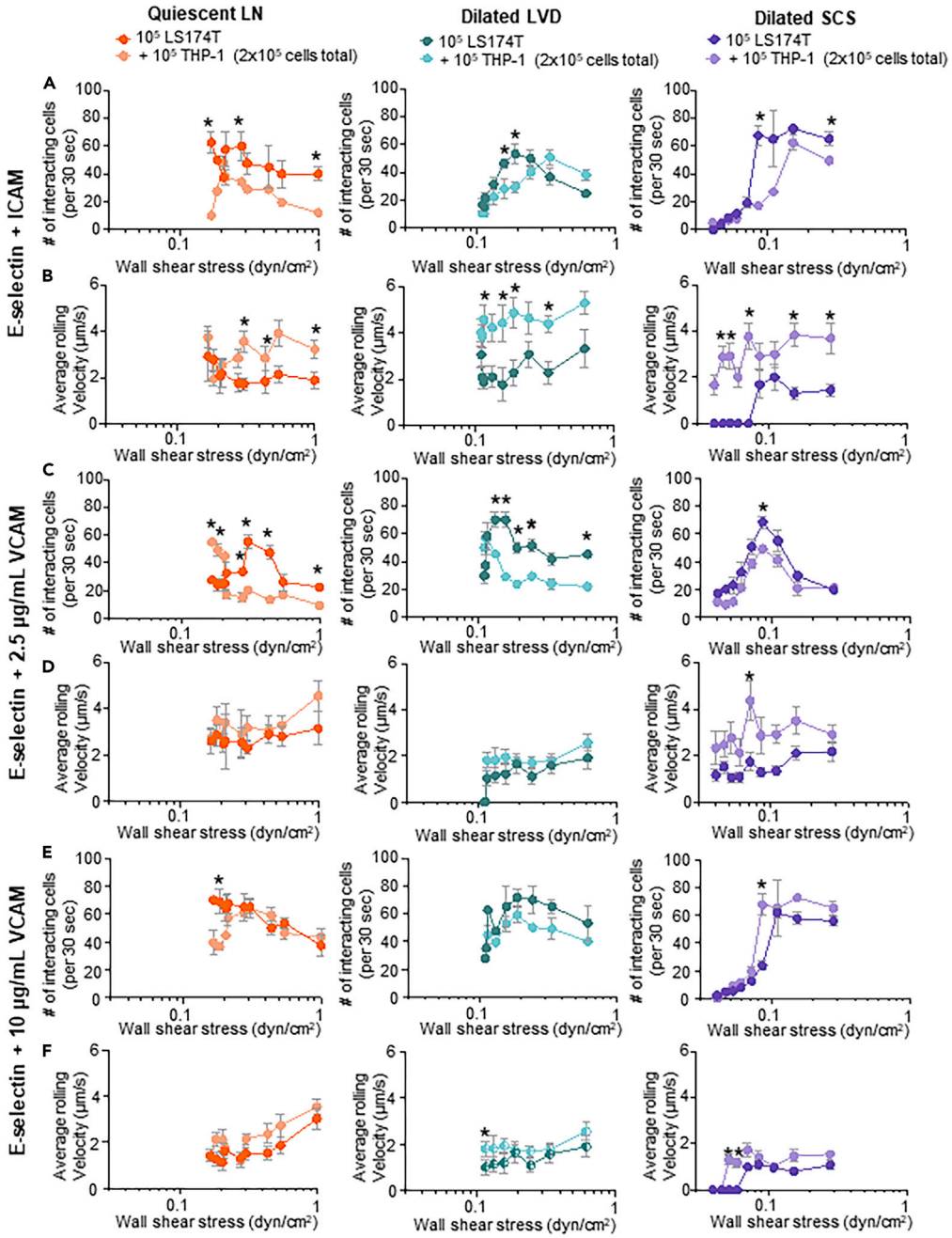

Figure 9. Co-perfusion with THP-1 Cells Alters the WSS Dependency of Adhesion by LS174T Cells to E-Selectin Co-presented with ICAM or VCAM

The number (A, C, and E) and average rolling velocity (B, D, and F) of interacting LS174T cells perfused in a total of 125 uL perfusion media either alone (105 total) or as 50% LS174T cells and 50% THP-1 cells (105 cells each) under flow conditions modeling quiescent LN (orange), dilated LVD (blue), or dilated SCS (purple) WSS levels. Channels were functionalized with 2.5 µg/mL E-selectin + 2.5 µg/mL ICAM (A,B), + 2.5 µg/mL VCAM (C and D), or + 10 µg/mL VCAM (E andF). Data are presented as mean ± SEM. * indicates significance by two-way ANOVA with Tukey post-hoc test.

interactions by THP-1 cells to ICAM with P-selectin that, as E-selectin, mediates rolling adhesion in flow (Edwards and Thomas, 2017). We found rolling adhesion velocity to diminish and ICAM co-presentation to mediate the accumulation of adhesive cells over channel lengths in a manner that was WSS dependent (Edwards et al., 2017). This suggests that the area of adhesive ligand presentation has the potential to regulate

crosstalk between transiting cells and adhesive substrate with respect to signaling or as we demonstrated, secondary cell adhesion in flow (Edwards et al., 2017).

Although these previous investigations focused on flow contexts with continuous WSS levels, the potential influence of diminishing WSS predicted to occur within the LN SCS microenvironment was explored herein. By altering the initial interactions of cells with adhesive substrates, diminished WSS levels in flow regimes mimicking remodeled LNs and context of adhesive ligand presentation were found to shape the trajectories and total extents of E-selectin-mediated cell adhesion over the perfusion channel length. This is unsurprising because, save the shear threshold effect, adhesion likelihood generally increases with diminishing WSS (Edwards and Thomas, 2017; Li et al., 2016). Cell adhesive behaviors, such as single molecule interactions, also depend in part on history of prior adhesion and cell-cell interactions (Edwards and Thomas, 2017). Lower levels of WSS encountered by cells upon entry into the functionalized channel portion in flows mimicking remodeled LNs thus facilitated locally higher levels of adhesion that, in most instances, decreased along the channel length in the direction of flow. This diminution may result in part due to cells in rolling adhesion transiting the channel at lower velocities, which remained unaffected by perfusion configuration, or also increased secondary adhesion resulting from higher initial adhesion extents. Notably, the channel position of maximal cell adhesion on E-selectin alone versus when co-presented with 10 μg/mL VCAM, which overall mediate the fastest versus slowest velocities of rolling adhesion, respectively, exhibited a direct versus inverse relationship with initial adhesion extent at the channel inlet irrespective of analyzed cell type. In the context of adhesion to E-selectin alone, however, this direct relationship diverged between models of quiescent versus inflamed LN flows, motivating future studies to unfurl the individual effects of WSS magnitude versus rate of dissipation to individually alter the dynamics of cell adhesion in shear flow. Overall, these findings suggest the influences of flow regime and adhesive ligand presentation on WSS magnitude, the length of adhesive substrate contact, and rolling velocity interdependently regulate cell adhesion in flow fields relevant to LN metastasis.

Immunoglobulin family members ICAM and VCAM are widely implicated in mediating immune cell migration into and through peripheral tissue lymphatics (Faveeuw et al., 2000; Harjunpää et al., 2019). Their expression is also correlated clinically with increased LN metastases in a variety cancers (Schlesinger and Bendas, 2015; Yan et al., 2014) and adhesion by colon adenocarcinoma cells to lymphatic endothelial cells *in vitro* (Kawai et al., 2012). Our results illustrate a potential means by which ICAM and VCAM may enable cancerous and monocytic cell homing to LNs by modulating the extent and dynamics of adhesion within the SCS. *In vitro* adhesion to ICAM and VCAM in the context of physiologically relevant fluid flow necessitated co-presentation with E-selectin, as would be expected given the synergistic role selectins play in adhesion initiation in shear flow environments (Burns and DePaola, 2005; Prabhakarpandian et al., 2001). This also helps contribute understanding to the previous observations of the involvement of E-selectin and other cell adhesion molecules in lymphatic metastasis in mouse models (Shaker et al., 2006; Steele, 2016; Zhu et al., 2018). In the context of lymphatic metastasis, this has not been clearly delineated but is supported by observations of correlation between the expression of these adhesion molecules and the incidence of LN metastasis (Schlesinger and Bendas, 2015; Yan et al., 2014).

Monocytes home to the LN via the afferent lymphatic vessel into the SCS and play a crucial role in mounting an immune response against disease (Evani et al., 2013; Ingersoll et al., 2011; Lund et al., 2016b). Prior work elucidating regulatory mechanisms of this migration pathway have focused on monocyte activation state, chemotactic cues, or adhesion molecule expression by the lymphatic endothelium within peripheral tissues (Shi and Pamer, 2011; Yang et al., 2014). Results from this work using monocytic THP-1 cells suggest the potential for homing by monocytes to LNs to also be regulated at the level of the LN itself, with respect to both locally presented adhesive cues as well as remodeling that may occur as a result of inflammation or disease. Monocytes are additionally implicated in metastatic dissemination by promoting colon cancer extravasation and the formation of lung metastases (Evani et al., 2013; Häuselmann et al., 2016). Monocytes also mediate and increase the adhesive behavior of cancer cells under flow (Evani et al., 2013; Häuselmann et al., 2016) with co-perfusion with cancer cells resulting in co-activation (Evani et al., 2013), suggestive of cell-cell cross-talk regulating adhesion in flow. In line with this, we found adhesion by metastatic LS174T cells to E-selectin in flow to be enhanced by co-perfusion with THP-1 cells in a manner not resultant from altered sterics/cell collisions and the WSS dependency of which was further influenced by both flow microenvironment and ICAM or VCAM co-presentation. This supports previous reports of monocytes

increasing cancer cell extravasation and metastatic tumor formation in LNs *in vivo* (Evani et al., 2013; Häuselmann et al., 2016).

In summary, a LN sinus microenvironment-mimicking microfluidic platform was developed to enable the *in vitro* interrogation of how different dissipating WSS flow models estimated to occur as a result of LN remodeling in response to disease or inflammation influence the adhesivity of cancerous and monocytic human cells in flow. Our results elaborate the influence of LN SCS flow microenvironment on the WSS dependencies of E-selectin-enabled adhesion extent but not rolling velocity magnitude, effects regulated interdependently by context of ICAM and/or VCAM co-presentation. These findings implicate the biophysical effects of LN remodeling as a potential axis regulating the mechanisms of LN invasion negatively implicated in cancer patient outcomes.

Limitations of the Study

Limitations of this work include the omission of lymphatic flow rates as a considered variable despite it being widely hypothesized that they are substantially changed in disease contexts (Habenicht et al., 2017; Hinson et al., 2017; Ji, 2017; Otto et al., 2014; Stacker et al., 2014; Sun et al., 2019). Given that the dependencies of WSS on SCS height and volumetric flow rate are first versus second order, respectively, we focused instead on how small changes with respect to SCS height could influence cell interactions within the SCS under the influence of fluid flow. The pulsatile nature of lymphatic flow was also not considered in the experimentally implemented perfusion regimes. In addition, levels of adhesion receptor expression within LNs *in vivo* have not been quantified, nor were densities of adhesive ligands on functionalized surfaces used for *in vitro* experimentation conducted here. The biochemical composition of the *in vitro* perfusion system is thus not necessarily physiological. Finally, the lymphatic vessel was approximated as entering the SCS at a 90° angle, resulting in uniform radial flow; however, the angle at which this vessel enters the SCS may vary significantly, making radially non-uniform flow.

Resource Availability

Lead Contact

Further information and requests for resources and reagents should be directed to and will be fulfilled by the Lead Contact, Susan Thomas (susan.thomas@gatech.edu).

Materials Availability

All materials (cell lines) can be obtained via MTA.

Data and Code Availability

The published article includes all data generated or analyzed during this study.

METHODS

All methods can be found in the accompanying Transparent Methods supplemental file.

SUPPLEMENTAL INFORMATION

Supplemental Information can be found online at https://doi.org/10.1016/j.isci.2020.101751.

ACKNOWLEDGMENTS

Funding: This work was supported by National Institutes of Health (NIH) grants R01CA207619, R21CA202849, P30CA16058, and T32GM008433, a President's Undergraduate Research Award from Georgia Tech, and the National Science Foundation Research Experience for Undergraduate through Georgia Tech's Summer Undergraduate Research Education program. The content is solely the responsibility of the authors and does not necessarily represent the official views of the National Institutes of Health.

AUTHOR CONTRIBUTIONS

Conceptualization, S.N.T.; Methodology, S.N.T., K.G.B., S.B., and D.R.A.; Formal Analysis, S.N.T., K.G.B., S.B., D.R.A., and M.J.O.; Investigation, K.G.B. and S.B.; Resources, M.J.O. and G.L.; Writing—Original

Draft, S.N.T. and K.G.B.; Writing—Review & Editing, S.N.T., K.G.B., and M.J.O.; Visualization, K.G.B. and S.N.T.; Funding Acquisition, S.N.T., B.E., G.L., and M.J.O..

DECLARATION OF INTERESTS

The authors declare no competing interests.

Received: May 17, 2020
Revised: October 11, 2020
Accepted: October 27, 2020
Published: November 20, 2020

REFERENCES

Achen, M.G., and Stacker, S.A. (2008). Molecular control of lymphatic metastasis. Ann. N Y Acad. Sci. *1131*, 225–234.

Berendam, S.J., Koeppel, A.F., Godfrey, N.R., Rouhani, S.J., Woods, A.N., Rodriguez, A.B., Peske, J.D., Cummings, K.L., Turner, S.D., and Engelhard, V.H. (2019). Comparative transcriptomic analysis identifies a range of immunologically related functional elaborations of lymph node associated lymphatic and blood endothelial cells. Front. Immunol. *10*, 816.

Birmingham, K.G., O'Melia, M.J., Ban, D., Mouw, J., Edwards, E.E., Marcus, A.I., McDonald, J., and Thomas, S.N. (2019). Analyzing mechanisms of metastatic cancer cell adhesive phenotype leveraging preparative adhesion chromatography microfluidic. Adv. Biosyst. *3*, 1800328.

Birmingham, K.G., Robinson, I.E., Edwards, E.E., and Thomas, S.N. (2020). Photoconversion and chromatographic microfluidic system reveals differential cellular phenotypes of adhesion velocity versus persistence in shear flow. Lab Chip *20*, 806–822.

Boscacci, R.T., Pfeiffer, F., Gollmer, K., Sevilla, A.I.C., Martin, A.M., Soriano, S.F., Natale, D., Henrickson, S., von Andrian, U.H., Fukui, Y., et al. (2010). Comprehensive analysis of lymph node stroma-expressed Ig superfamily members reveals redundant and nonredundant roles for ICAM-1, ICAM-2, and VCAM-1 in lymphocyte homing. Blood *116*, 915–925.

Burns, M.P., and DePaola, N. (2005). Flow-conditioned HUVECs support clustered leukocyte adhesion by coexpressing ICAM-1 and E-selectin. Am. J. Physiol. Heart Circ. Physiol. *288*, H194–H204.

Carr, I. (1983). Lymphatic metastasis. Cancer Metastasis Rev. *2*, 307–317.

Dalal, P.U., Sohaib, S.A., and Huddart. (2006). Imaging of testicular germ cell tumours. Cancer Imaging *6*, 124–134.

Dallas, M.R., Liu, G., Chen, W.-C., Thomas, S.N., Wirtz, D., Huso, D.L., and Konstantopoulos, K. (2012). Divergent roles of CD44 and carcinoembryonic antigen in colon cancer metastasis. FASEB J. *26*, 2648–2656.

Das, S., Sarrou, E., Podgrabinska, S., Cassella, M., Mungamuri, S.K., Feirt, N., Gordon, R., Nagi, C.S., Wang, Y., Entenberg, D., et al. (2013). Tumor cell entry into the lymph node is controlled by CCL1 chemokine expressed by lymph node lymphatic sinuses. J. Exp. Med. *210*, 1509–1528.

Delitto, D., Judge, S.M., Delitto, A.E., Nosacka, R.L., Rocha, F.G., DiVita, B.B., Gerber, M.H., George, T.J., Behrns, K.E., Hughes, S.J., et al. (2017). Human pancreatic cancer xenografts recapitulate key aspects of cancer cachexia. Oncotarget *8*, 1177–1189.

Dixon, J.B., Greiner, S.T., Gashev, A.A., Cote, G.L., Moore, J.E., and Zawieja, D.C. (2006). Lymph flow, shear stress, and lymphocyte velocity in rat mesenteric prenodal lymphatics. Microcirculation *13*, 597–610.

Edwards, E.E., Birmingham, K.G., O'Melia, M.J., Oh, J., and Thomas, S.N. (2018). Fluorometric quantification of single cell velocities to investigate cancer metastasis. Cell Systems *7*, 496–509.

Edwards, E.E., Oh, J., Anilkumar, A., Birmingham, K.G., and Thomas, S.N. (2017). P-, but not E- or L-, selectin-mediated rolling adhesion persistence in hemodynamic flow diverges between metastatic and leukocytic cells. Oncotarget *8*, 83585–83601.

Edwards, E.E., and Thomas, S.N. (2017). P-Selectin and ICAM-1 synergy in mediating THP-1 monocyte adhesion in hemodynamic flow is length dependent. Integr. Biol. (Camb) *9*, 313–327.

Elmore, S.A. (2006). Histopathology of the lymph nodes. Toxicol. Pathol. *34*, 425–454.

Emir, E.E., Qureshi, U., Dearling, J.L.J., Boxer, G.M., Clatworthy, I., Folarin, A.A., Robson, M.P., Nagl, S., Konerding, M.A., and Pedley, R.B. (2007). Predicting response to radioimmunotherapy from the tumor microenvironment of colorectal carcinomas. Cancer Res. *67*, 11896–11905.

Evani, S.J., Prabhu, R.G., Gnanaruban, V., Finol, E.A., and Ramasubramanian, A.K. (2013). Monocytes mediate metastatic breast tumor cell adhesion to endothelium under flow. FASEB J. *27*, 3017–3029.

Fan, Y., Gan, Y., Shen, Y., Cai, X., Song, Y., Zhao, F., Yao, M., Gu, J., and Tu, H. (2015). Leptin signaling enhances cell invasion and promotes the metastasis of human pancreatic cancer via increasing MMP-13 production. Oncotarget *6*, 16120–16134.

Faveeuw, C., Di Mauro, M.E., Price, A.A., and Ager, A. (2000). Roles of α4 integrins/VCAM-1 and LFA-1/ICAM-1 in the binding and transendothelial migration of T lymphocytes and T lymphoblasts across high endothelial venules. Int. Immunol. *12*, 241–251.

Fontebasso, Y., and Dubinett, S.M. (2015). Drug development for metastasis prevention. Crit. Rev. Oncog *20*, 449–473.

Fortea-Sanchis, C., Martínez-Ramos, D., and Escrig-Sos, J. (2018). The lymph node status as a prognostic factor in colon cancer: comparative population study of classifications using the logarithm of the ratio between metastatic and nonmetastatic nodes (LODDS) versus the pN-TNM classification and ganglion ratio systems. BMC Cancer *18*, 1208.

Fujisaki, T., Tanaka, Y., Fujii, K., Mine, S., Saito, K., Yamada, S., Yamashita, U., Irimura, T., and Eto, S. (1999). CD44 stimulation induces integrin-mediated adhesion of colon cancer cell lines to endothelial cells by up-regulation of integrins and c-met and activation of integrins. Cancer Res. *59*, 4427–4434.

Fujiwara, M., Sawada, M., Kasuya, A., Matsushita, Y., Yamada, M., Fukamizu, H., Magata, Y., Tokura, Y., and Sakahara, H. (2014). Measurement of cutaneous lymphatic flow rates in patients with skin cancer: area extraction method. J. Dermatol. *41*, 498–504.

Habenicht, L.M., Kirschbaum, S.B., Furuya, M., Harrell, M.I., and Ruddell, A. (2017). Tumor regulation of lymph node lymphatic sinus growth and lymph flow in mice and in humans. Yale J. Biol. Med. *90*, 403–415.

Hampton, H.R., and Chtanova, T. (2019). Lymphatic migration of immune cells. Front. Immunol. *10*, 1168.

Hanley, W.D., Napier, S.L., Burdick, M.M., Schnaar, R.L., Sackstein, R., and Konstantopoulos, K. (2006). Variant isoforms of CD44 are P- and L-selectin ligands on colon carcinoma cells. FASEB J. *20*, 337–339.

Harjunpää, H., Llort Asens, M., Guenther, C., and Fagerholm, S.C. (2019). Cell adhesion molecules and their roles and regulation in the immune and tumor microenvironment. Front. Immunol. *10*, 1078.

Harmsen, A.G., Muggenburg, B.A., Snipes, M.B., and Bice, D.E. (1985). The role of macrophages in particle translocation from lungs to lymph nodes. Science *230*, 1277–1280.

Harrell, M.I., Iritani, B.M., and Ruddell, A. (2007). Tumor-induced sentinel lymph node lymphangiogenesis and increased lymph flow precede melanoma metastasis. Am. J. Pathol. *170*, 774–786.

Häuselmann, I., Roblek, M., Protsyuk, D., Huck, V., Knopfova, L., Grässle, S., Bauer, A.T., Schneider, S.W., and Borsig, L. (2016). Monocyte induction of E-selectin-mediated endothelial activation releases VE-cadherin junctions to promote tumor cell extravasation in the metastasis cascade. Cancer Res. *76*, 5302–5312.

Hinson, A.M., Massoll, N.A., Ann Jolly, L., Stack, B.C., Jr., Bodenner, D.L., and Franco, A.T. (2017). Structural alterations in tumor-draining lymph nodes before papillary thyroid carcinoma metastasis. Head Neck *39*, 1639–1646.

Hoshida, T., Isaka, N., Hagendoorn, J., di Tomaso, E., Chen, Y.-L., Pytowski, B., Fukumura, D., Padera, T.P., and Jain, R.K. (2006). Imaging steps of lymphatic metastasis reveals that vascular endothelial growth factor-C increases metastasis by increasing delivery of cancer cells to lymph nodes: therapeutic implications. Cancer Res. *66*, 8065–8075.

Huang, Q., Hu, X., He, W., Zhao, Y., Hao, S., Wu, Q., Li, S., Zhang, S., and Shi, M. (2018). Fluid shear stress and tumor metastasis. Am. J. Cancer Res. *8*, 763–777.

Ingersoll, M.A., Platt, A.M., Potteaux, S., and Randolph, G.J. (2011). Monocyte trafficking in acute and chronic inflammation. Trends Immunol. *32*, 470–477.

Jadhav, S., Bochner, B.S., and Konstantopoulos, K. (2001). Hydrodynamic shear regulates the kinetics and receptor specificity of polymorphonuclear leukocyte-colon carcinoma cell adhesive interactions. J. Immunol. *167*, 5986–5993.

Jafarnejad, M., Woodruff, M.C., Zawieja, D.C., Carroll, M.C., and Moore, J.E. (2015). Modeling lymph flow and fluid exchange with blood vessels in lymph nodes. Lymphat Res. Biol. *13*, 234–247.

Jakubzick, C., Gautier, E.L., Gibbings, S.L., Sojka, D.K., Schlitzer, A., Johnson, T.E., Ivanov, S., Duan, Q., Bala, S., Condon, T., et al. (2013). Minimal differentiation of classical monocytes as they survey steady-state tissues and transport antigen to lymph nodes. Immunity *39*, 599–610.

Jeong, K., Murphy, J.M., Rodriguez, Y.A.R., Kim, J.-S., Ahn, E.-Y.E., and Lim, S.-T.S. (2019). FAK inhibition reduces metastasis of α4 integrin-expressing melanoma to lymph nodes by targeting lymphatic VCAM-1 expression. Biochem. Biophys. Res. Commun. *509*, 1034–1040.

Ji, R.-C. (2017). Lymph nodes and cancer metastasis: new perspectives on the role of intranodal lymphatic sinuses. Int. J. Mol. Sci. *18*, 51.

Jones, D.A., McIntire, L.V., Smith, C.W., and Picker, L.J. (1994). A two-step adhesion cascade for T cell/endothelial cell interactions under flow conditions. J. Clin. Invest. *94*, 2443–2450.

Karaman, S., and Detmar, M. (2014). Mechanisms of lymphatic metastasis. J. Clin. Invest. *124*, 922–928.

Karnezis, T., Shayan, R., Caesar, C., Roufail, S., Harris, N.C., Ardipradja, K., Zhang, Y.F., Williams, S.P., Farnsworth, R.H., Chai, M.G., et al. (2012). VEGF-D promotes tumor metastasis by regulating prostaglandins produced by the collecting lymphatic endothelium. Cancer Cell *21*, 181–195.

Kate, M., Hofland, L.J., van Koetsveld, P.M., Jeekel, J., and van Eijck, C.H.J. (2006). Pro-inflammatory cytokines affect pancreatic carcinoma cell. Endothelial cell interactions. JOP *7*, 454–464.

Kawai, Y., Kaidoh, M., Yokoyama, Y., and Ohhashi, T. (2012). Pivotal roles of shear stress in the microenvironmental changes that occur within sentinel lymph nodes. Cancer Sci. *103*, 1245–1252.

Kawai, Y., Kaidoh, M., Yokoyama, Y., Sano, K., and Ohhashi, T. (2009). Chemokine CCL2 facilitates ICAM-1-mediated interactions of cancer cells and lymphatic endothelial cells in sentinel lymph nodes. Cancer Sci. *100*, 419–428.

Kong, D.-H., Kim, Y.K., Kim, M.R., Jang, J.H., and Lee, S. (2018). Emerging roles of vascular cell adhesion molecule-1 (VCAM-1) in immunological disorders and cancer. Int. J. Mol. Sci. *19*, 1057.

Lee, Y.-C., Jin, J.-K., Cheng, C.-J., Huang, C.-F., Song, J.H., Huang, M., Brown, W.S., Zhang, S., Yu-Lee, L.-Y., Yeh, E.T., et al. (2013). Targeting constitutively activated β 1 integrins inhibits prostate cancer metastasis. Mol. Cancer Res. *11*, 405–417.

Leirião, P., del Fresno, C., and Ardavín, C. (2012). Monocytes as effector cells: activated Ly-6Chigh mouse monocytes migrate to the lymph nodes through the lymph and cross-present antigens to CD8+ T cells. Eur. J. Immunol. *42*, 2042–2051.

León, B., López-Bravo, M., and Ardavín, C. (2007). Monocyte-derived dendritic cells formed at the infection site control the induction of protective T helper 1 responses against Leishmania. Immunity *26*, 519–531.

Li, Q., Wayman, A., Lin, J., Fang, Y., Zhu, C., and Wu, J. (2016). Flow-enhanced stability of rolling adhesion through E-selectin. Biophys. J. *111*, 686–699.

López, S., Prats, N., and Marco, A.J. (1999). Expression of E-selectin, P-selectin, and intercellular adhesion molecule-1 during experimental murine listeriosis. Am. J. Pathol. *155*, 1391–1397.

Lund, A.W., Medler, T.R., Leachman, S.A., and Coussens, L.M. (2016a). Lymphatic vessels, inflammation, and immunity in skin cancer. Cancer Discov. *6*, 22–35.

Lund, H., Boysen, P., Åkesson, C.P., Lewandowska-Sabat, A.M., and Storset, A.K. (2016b). Transient migration of large numbers of CD14++ CD16+ monocytes to the draining lymph node after onset of inflammation. Front. Immunol. *7*, 322.

Makkouk, A., and Weiner, G.J. (2015). Cancer immunotherapy and breaking immune tolerance: new approaches to an old challenge. Cancer Res. *75*, 5–10.

Maletto, B.A., Ropolo, A.S., Alignani, D.O., Liscovsky, M.V., Ranocchia, R.P., Moron, V.G., and Pistoresi-Palencia, M.C. (2006). Presence of neutrophil-bearing antigen in lymphoid organs of immune mice. Blood *108*, 3094–3102.

McCarty, O.J., Mousa, S.A., Bray, P.F., and Konstantopoulos, K. (2000). Immobilized platelets support human colon carcinoma cell tethering, rolling, and firm adhesion under dynamic flow conditions. Blood *96*, 1789–1797.

McLaughlin, R.A., Scolaro, L., Robbins, P., Hamza, S., Saunders, C., and Sampson, D.D. (2010). Imaging of human lymph nodes using optical coherence tomography: potential for staging cancer. Cancer Res. *70*, 2579–2584.

Miyaji, K., Furuse, A., Nakajima, J., Kohno, T., Ohtsuka, T., Yagyu, K., Oka, T., and Omata, S. (1997). The stiffness of lymph nodes containing lung carcinoma metastases: a new diagnostic parameter measured by a tactile sensor. Cancer *80*, 1920–1925.

Moore, J.E., and Bertram, C.D. (2018). Lymphatic system flows. Annu. Rev. Fluid Mech. *50*, 459–482.

Nakashima, H., Terabe, M., Berzofsky, J., Husain, S., and Puri, R. (2011). A novel combination immunotherapy for cancer by IL-13r 2-targeted DNA vaccine and immunotoxin in murine tumor models. J. Immunol. *187*, 4935–4946.

Nakayama, A., Ogawa, A., Fukuta, Y., and Kudo, K. (1999). Relation between lymphatic vessel diameter and clinicopathologic parameters in squamous cell carcinomas of the oral region. Cancer *86*, 200–206.

Oh, J., Edwards, E.E., McClatchey, P.M., and Thomas, S.N. (2015). Analytical cell adhesion chromatography reveals impaired persistence of metastatic cell rolling adhesion to P-selectin. J. Cell Sci. *128*, 3731–3743.

Ohtani, O., and Ohtani, Y. (2008). Structure and function of rat lymph nodes. Arch. Histol. Cytol. *71*, 69–76.

Otto, B., Koenig, A.M., Tolstonog, G.V., Jeschke, A., Klaetschke, K., Vashist, Y.K., Wicklein, D., Wagener, C., Izbicki, J.R., and Streichert, T. (2014). Molecular changes in pre-metastatic lymph nodes of esophageal cancer patients. PLoS One *9*, e102552.

Ozasa, R., Ohno, J., Iwahashi, T., and Taniguchi, K. (2012). Tumor-induced lymphangiogenesis in cervical lymph nodes in oral melanoma-bearing mice. J. Exp. Clin. Cancer Res. *31*, 83.

Pai, R.K., Beck, A.H., Mitchem, J., Linehan, D.C., Chang, D.T., Norton, J.A., and Pai, R.K. (2011). Pattern of lymph node involvement and prognosis in pancreatic adenocarcinoma: direct lymph node invasion has similar survival to node-negative disease. Am. J. Surg. Pathol. *35*, 228–234.

Pan, W.-R., le Roux, C.M., Levy, S.M., and Briggs, C.A. (2010). The morphology of the human lymphatic vessels in the head and neck. Clin. Anat. *23*, 654–661.

Paschos, K.A., Canovas, D., and Bird, N.C. (2010). The engagement of selectins and their ligands in colorectal cancer liver metastases. J. Cell. Mol. Med. *14*, 165–174.

Paszek, M.J., Zahir, N., Johnson, K.R., Lakins, J.N., Rozenberg, G.I., Gefen, A., Reinhart-King, C.A., Margulies, S.S., Dembo, M., Boettiger, D., et al. (2005). Tensional homeostasis and the malignant phenotype. Cancer Cell *8*, 241–254.

Planas-Paz, and Lammert, E. (2014). Mechanosensing in developing lymphatic vessels. Adv. Anat. Embryol. Cell Biol. *214*, 23–40.

Prabhakarpandian, B., Goetz, D.J., Swerlick, R.A., Chen, X., and Kiani, M.F. (2001). Expression and functional significance of adhesion molecules on cultured endothelial cells in response to ionizing radiation. Microcirculation *8*, 355–364.

Randolph, G.J., Inaba, K., Robbiani, D.F., Steinman, R.M., and Muller, W.A. (1999). Differentiation of phagocytic monocytes into lymph node dendritic cells in vivo. Immunity *11*, 753–761.

Rebhun, R.B., Cheng, H., Gershenwald, J.E., Fan, D., Fidler, I.J., and Langley, R.R. (2010). Constitutive expression of the α4 integrin correlates with tumorigenicity and lymph node metastasis of the B16 murine melanoma. Neoplasia *12*, 173–182.

Riedel, A., Shorthouse, D., Haas, L., Hall, B.A., and Shields, J. (2016). Tumor-induced stromal reprogramming drives lymph node transformation. Nat. Immunol. *17*, 1118–1127.

Rohner, N.A., McClain, J., Tuell, S.L., Warner, A., Smith, B., Yun, Y., Mohan, A., Sushnitha, M., and Thomas, S.N. (2015). Lymph node biophysical remodeling is associated with melanoma lymphatic drainage. FASEB J. *29*, 4512–4522.

Scallan, J.P., Zawieja, S.D., Castorena-Gonzalez, J.A., and Davis, M.J. (2016). Lymphatic pumping: mechanics, mechanisms and malfunction. J. Physiol. *594*, 5749–5768.

Schlesinger, M., and Bendas, G. (2015). Vascular cell adhesion molecule-1 (VCAM-1)–an increasing insight into its role in tumorigenicity and metastasis. Int. J. Cancer *136*, 2504–2514.

Seidl, M., Bader, M., Vaihinger, A., Wellner, U.F., Todorova, R., Herde, B., Schrenk, K., Maurer, J., Schilling, O., Erbes, T., et al. (2018). Morphology of immunomodulation in breast cancer tumor draining lymph nodes depends on stage and intrinsic subtype. Sci. Rep. *8*, 5321.

Shaker, O.G., Ay El-Deen, M.A., Abd El-Rahim, M.T., and Talaat, R.M. (2006). Gene expression of E-selectin in tissue and its protein level in serum of breast cancer patients. Tumori *92*, 524–530.

Shi, C., and Pamer, E.G. (2011). Monocyte recruitment during infection and inflammation. Nat. Rev. Immunol. *11*, 762–774.

Singh, R., and Choi, B.K. (2019). Siglec1-expressing subcapsular sinus macrophages provide soil for melanoma lymph node metastasis. eLife *8*, e48916.

Sleeman, J.P., Nazarenko, I., and Thiele, W. (2011). Do all roads lead to Rome? Routes to metastasis development. Int. J. Cancer *128*, 2511–2526.

Stacker, S.A., Williams, S.P., Karnezis, T., Shayan, R., Fox, S.B., and Achen, M.G. (2014). Lymphangiogenesis and lymphatic vessel remodelling in cancer. Nat. Rev. Cancer *14*, 159–172.

Steele, M. (2016). Pancreatic cancer invasion of the lymphatic vasculature and contributions of the tumor microenvironment: roles for E-selectin and CXCR4. Theses Dissertations *166*, 1–191.

Sun, B., Zhou, Y., Fang, Y., Li, Z., Gu, X., and Xiang, J. (2019). Colorectal cancer exosomes induce lymphatic network remodeling in lymph nodes. Int. J. Cancer *145*, 1648–1659.

Swartz, M.A., and Lund, A.W. (2012). Lymphatic and interstitial flow in the tumour microenvironment: linking mechanobiology with immunity. Nat. Rev. Cancer *12*, 210–219.

Sweety, S.V., and Narayankar, A.S. (2019). Evaluation of lymph node ratio and morphologic patterns of nodal reactive hyperplasia in primary organ malignancy. Indian J. Pathol. Microbiol. *62*, 216–221.

Thomas, S.N., Zhu, F., Schnaar, R.L., Alves, C.S., and Konstantopoulos, K. (2008). Carcinoembryonic antigen and CD44 variant isoforms cooperate to mediate colon carcinoma cell adhesion to E- and L-selectin in shear flow. J. Biol. Chem. *283*, 15647–15655.

Trevaskis, N.L., Kaminskas, L.M., and Porter, C.J.H. (2015). From sewer to saviour - targeting the lymphatic system to promote drug exposure and activity. Nat. Rev. Drug Discov. *14*, 781–803.

Turner, V.M., and Mabbott, N.A. (2017). Structural and functional changes to lymph nodes in ageing mice. Immunology *151*, 239–247.

Vigl, B., Aebischer, D., Nitschké, M., Iolyeva, M., Röthlin, T., Antsiferova, O., and Halin, C. (2011). Tissue inflammation modulates gene expression of lymphatic endothelial cells and dendritic cell migration in a stimulus-dependent manner. Blood *118*, 205–215.

Vinay, D.S., Ryan, E.P., Pawelec, G., Talib, W.H., Stagg, J., Elkord, E., Lichtor, T., Decker, W.K., Whelan, R.L., Kumara, H.M.C.S., et al. (2015). Immune evasion in cancer: mechanistic basis and therapeutic strategies. Semin. Cancer Biol. *35*, S185–S198.

Webster, B., Ekland, E.H., Agle, L.M., Chyou, S., Ruggieri, R., and Lu, T.T. (2006). Regulation of lymph node vascular growth by dendritic cells. J. Exp. Med. *203*, 1903–1913.

Weledji, E.P., Enoworock, G., Mokake, M., and Sinju, M. (2016). How Grim is pancreatic cancer? Oncol. Rev. *10*, 294.

West, H., and Jin, J. (2016). Lymph nodes and lymphadenopathy in cancer. JAMA Oncol. *2*, 971.

Wirtz, D., Konstantopoulos, K., and Searson, P.C. (2011). The physics of cancer: the role of physical interactions and mechanical forces in metastasis. Nat. Rev. Cancer *11*, 512–522.

Wong, S.L. (2009). Lymph node counts and survival rates after resection for colon and rectal cancer. Gastrointest. Cancer Res. *3*, S33–S35.

Wong, S.Y., and Hynes, R.O. (2006). Lymphatic or hematogenous dissemination: how does a metastatic tumor cell decide? Cell Cycle *5*, 812–817.

Yago, T., Tsukuda, M., and Minami, M. (1999). P-selectin binding promotes the adhesion of monocytes to VCAM-1 under flow conditions. J. Immunol. *163*, 367–373.

Yan, J., Jiang, Y., Ye, M., Liu, W., and Feng, L. (2014). The clinical value of lymphatic vessel density, intercellular adhesion molecule 1 and vascular cell adhesion molecule 1 expression in patients with oral tongue squamous cell carcinoma. J. Cancer Res. Ther. *10*, 125–130.

Yang, J., Zhang, L., Yu, C., Yang, X.-F., and Wang, H. (2014). Monocyte and macrophage differentiation: circulation inflammatory monocyte as biomarker for inflammatory diseases. Biomark Res. *2*, 1.

You, M.S., Lee, S.H., Choi, Y.H., Shin, B., Paik, W.H., Ryu, J.K., Kim, Y.-T., Jang, D.K., Lee, J.K., Kwon, W., et al. (2019). Lymph node ratio as valuable predictor in pancreatic cancer treated with R0 resection and adjuvant treatment. BMC Cancer *19*, 952.

Zhang, Z., Procissi, D., Li, W., Kim, D.-H., Li, K., Han, G., Huan, Y., and Larson, A.C. (2013). High resolution MRI for non-invasive mouse lymph node mapping. J. Immunol. Methods *400-401*, 23–29.

Zhu, T., Hu, X., Wei, P., and Shan, G. (2018). Molecular background of the regional lymph node metastasis of gastric cancer. Oncol. Lett. *15*, 3409–3414.

iScience, Volume *23*

Supplemental Information

Lymph Node Subcapsular Sinus Microenvironment-On-A-Chip Modeling Shear Flow Relevant to Lymphatic Metastasis and Immune Cell Homing

Katherine G. Birmingham, Meghan J. O'Melia, Samantha Bordy, David Reyes Aguilar, Bassel El-Reyas, Gregory Lesinski, and Susan N. Thomas

Transparent Methods

Cell Culture

THP-1 monocytes were cultured RPMI-1640 supplemented with 10% heat inactivated fetal bovine serum and 1% penicillin/streptomycin/amphotericin B. PANC-1 cells were cultured in Dulbecco's Modified Eagle Medium supplemented with 10% heat inactivated fetal bovine serum, 1% penicillin/streptomycin/amphotericin B, and 1% Glutamax. Parental and Phamret-expressing (Edwards et al., 2018) human colorectal adenocarcinoma LS174T cells were cultured in Dulbecco's Modified Eagle Medium supplemented with 10% heat inactivated fetal bovine serum and 1% penicillin/streptomycin/amphotericin B. For perfusion experiments, LS174T and PANC-1 cells were harvested via mild trypsinization with 0.25% trypsin/ethylenediaminetetraacetic acid, centrifuged at 400 X G for 5 min, resuspended in culture medium, and incubated in suspension for 2 h at 37°C to allow regeneration of adhesive cell surface ligands prior to centrifugation and resuspension in perfusion medium [0.1 % bovine serum albumin (BSA) in D-PBS with calcium and magnesium] and subsequent storage on ice until use (< 1 h). THP-1 cells were directly harvested (without trypsinization), centrifuged at 400 X G for 5 min, and resuspended in perfusion medium for storage on ice until use (< 1 h). B16F10 cells were cultured in Dulbecco's Modified Eagle Medium with 10% heat-inactivated fetal bovine serum and 1% penicillin/streptomycin/amphotericin B and harvested by trypsinization prior to use *in vivo* experimentation.

LN immunohistochemistry, imaging, and analysis

Brachial LNs from naïve C57Bl6 mice or draining melanomas 7 d post intradermal implantation in the lateral dorsal skin with $5x10^5$ B16F10 cells (Rohner et al., 2015) were surgically excised, embedded in optimum cutting temperature embedding medium, and stored at -80°C. A cryostat was used to slice 10 µm thick tissue sections that were mounted onto histological slides and stored at -20°C. Sections were acetone fixed for 20 min at -20°C, blocked with 10% goat serum diluted in Dulbecco's Phosphate Buffered Saline (D-PBS) with calcium and magnesium for 1 h at room temperature, and incubated overnight at 4°C with the following primary antibodies: (1) rabbit anti-mouse LYVE-1 (1:200, Invitrogen, PA1-16635), (2) chicken anti-mouse CD62E (1:100, Novus Biologicals, AF575), and (3) hamster anti-mouse CD54 (1:100, Novus Biologicals, NBP2-22540) or rat anti-mouse CD106 (1:50, Novus Biologicals, NB100-77474). The following day, the slides were incubated for 1 h at room temperature with the following fluorophore conjugated secondary antibodies: (1) goat anti-rabbit Alexa Flour 633 (1:300, Invitrogen, A-21070), (2) goat anti-chicken Alexa Flour 488 (1:200, Invitrogen, A-11039), and (3) goat anti-hamster DyLight 550 (1:1000, Novus Biologicals, NBP1-71730R) or goat anti-rat DyLight 550 (1:100, Invitrogen, SA5-10019). In between each staining step, slides were washed three times with gentle agitation in 0.1% Tween 20 diluted in D-PBS with calcium and magnesium. Washed slides were mounted using Vectashield mounting medium with DAPI and microscopic images were taken using a Zeiss 710 confocal microscope. Collagen structures of whole LNs pre-treated with increasing concentrations of 2-2' thiodiethanol (10, 25, 50, 97%) for 10-30 min prior to mounting in Fluorogel were imaged in 2 µm intervals up to a 100 µm tissue depth using two-photon microcroscopy collecting

the collagen second harmonic on a LSM 510 confocal microscope up to 100 um depth. SCS heights were measured using Zen Black Software.

COMSOL Modelling

WSS profiles along the SCS floors were modeled using COMSOL Multiphysics Software version 5.4. An idealized LN sinus was designed in SolidWorks, modeling the afferent lymphatic vessel as a cylinder leading fluid to radially disperse into the LN SCS modeled as a thin disk (Figure 2B). Various LN dimensions, including the afferent LVD and SCS height were used to construct three variations of the idealized LN luminal geometry (Figure 2B), while the upper limit of the SCS radius was maintained at 5 mm and 0.5 mm was chosen based on the average size of human and mouse LNs, respectively (Jafarnejad et al., 2015; Kikuchi et al., 2020; Takeda et al., 2017). LN geometries were exported as .STL files and imported into COMSOL. Within COMSOL, the fluid material was defined as a Newtonian, incompressible fluid with a dynamic viscosity of 1800 Pa s and density of 1009 kg m^{-3} (Moore and Bertram, 2018). The fluid flow was set to laminar flow with a constant volumetric flow rate of 1.33E-10 $m^3 s^{-1}$, which is within the range of flow rates observed in humans (Blatter et al., 2016). The boundary walls were chosen to be the outer surface of the liquid domain, the inlet was defined as the top of the afferent vessel cylinder, and the outlet was defined to be the circumferential side wall of the SCS thin disc. The boundaries were set as impermeable. Finally, the cut plane where the WSS values were quantified was defined as the bottom of the thin disc (z = 0, Figure 2I), representing the inferior floor of the LN SCS.

The Particle Tracing for Fluid Flow module of COMSOL Multiphysics Software version 5.4 was used to simulate cell trajectories during movement from the afferent vessel into the LN SCS and to determine the location at which cells were in close proximity with the inferior surface of the SCS. Particle properties were modeled after that of cancerous cells, with a diameter of 14 μm and a mass density of 1032 kg m^{-3} (Moore and Bertram, 2018). The same inlet, outlet, flow rate, fluid properties, and boundary walls as used in the WSS modeling described were used in particle trajectory simulations. For each simulation, a particle (cell) began its flow trajectory through the geometry at the top of the afferent vessel (2.5 mm from the SCS floor) in a randomly selected radial position (less than or equal to one half the diameter of the afferent vessel), and the height and radial position of the particle was tracked until it reached the periphery of the SCS. The particle was defined as settled on the SCS floor when the center of the particle was at a height of 7 μm, the particle radius.

Channel Fabrication

Microfluidic channels were fabricated in a manner similar to that detailed previously (Birmingham et al., 2019b; Erin Elizabeth Edwards et al., 2018; Tran et al., 2017). Briefly, the adhesive microfluidic channel, which consisted of a straight 10 cm long by 0.2 cm wide section connected to a 4 cm long divergent section that increased in width from 0.2 cm to 1.2 cm, was cut from sheet of 125 μm thick double-sided adhesive tape backed with a release liner. The channel was then affixed to polydimethylsiloxane, which was previously cured by mixing polydimethylsiloxane base with curing agent at a ratio of 9:1 and curing at 90˚C for 3 h in a Pyrex dish prior to being cut to the outer dimensions of the

channel shape. An inlet hole was punched into the beginning of the long, straight portion of the channel using a 3 mm biopsy punch, and the construct was attached to a non-tissue culture treated polystyrene plates into which an outlet hole was drilled prior to assembly.

Channel Functionalization

The short, divergent portion of the channel nearest the outlet was functionalized by incubation overnight at 4°C with Fc specific anti-IgG diluted in D-PBS without calcium and magnesium to a concentration of 2.5, 5, or 12.5 μg mL^{-1} for eventual use with E-selectin alone or in combination with 2.5 μg mL^{-1} ICAM or VCAM or 10 μg mL^{-1} VCAM experiments, respectfully. Next, plates were blocked for 1 h at room temperature with 1% BSA in D-PBS with calcium and magnesium after which E-selectin alone or in addition to either ICAM or VCAM diluted in D-PBS with calcium and magnesium was incubated for 2 h at room temperature. The entire channel was blocked for 1 h at room temperature with 1% BSA in D-PBS with calcium and magnesium at room temperature, after which plates were washed and immediately used in perfusion experiments. In between each step, the channel was washed three times with 1 mL of D-PBS with calcium and magnesium.

Perfusion Experiment Workflow

Perfusion experiments were performed in a similar manner to that formerly described (Birmingham et al., 2019b). Succinctly, an inlet syringe connected to tubing filled with perfusion media was connected to a syringe pump and used to withdraw a cell

pulse into the inlet tubing at a rate of 0.5 mL min^{-1}. For perfusion experiments using a single cell type, the cell pulse consisted of $2x10^5$ LS174T, PANC-1, or THP-1 cells diluted in 125 µL of perfusion media. The tubing and syringe assembly was inserted into the inlet hole of the channel and an outlet reservoir was made by connecting a 5 mL test tube to the bottom of the drilled outlet hole on the polystyrene plate. The assembled platform was placed on an Eclipse TI optical microscope with an objective magnification of 10X and linked to NIS-Elements software to acquire videos at a frame rate of 25 frames per sec at an exposure time of 0.281 µsec and 2x2 binning of a 500 by 376 pixels.

To begin perfusion, the syringe pump was set to a constant flow rate, based on desired WSS ranges of different LN flow models, to initiate inflow into the channel from the syringe-tubing assembly. Flow rates of 34.7, 27.4, and 9.7 mL min^{-1} were used to model quiescent LN, dilated LVD, and dilated SCS flows, respectively. Once cells reached the divergent portion of the channel during perfusion experiments, 30 sec videos were taken along the center line of the channel at 0.5 cm increments using the integrated Nikon camera. Perfusions were continued until all cells, except those that firmly adhered to the functionalized portion of the channel, eluted from the device as determined by the lack of any rolling cells within the functionalized portion as verified by videomicroscopy.

LS174T Cell and THP-1 Cell Coperfusion Workflow

For studies involving the co-perfusion of LS174T in combination with THP-1 cells, 125 µL total volume cell pulse was made by diluting 10^5 Phamret-expressing LS174T cells with 0, $0.33x10^5$, $1.0x10^5$, or $3.0x10^5$ THP-1 monocytes immediately before perfusion. Furthermore, the Phamret-expressing LS174T cells were pre-photoconverted

prior to perfusion to permit the visualization of the LS174T cells, but not the THP-1 cells, using a fluorescein isothiocyanate filter (Birmingham et al., 2020; Edwards et al., 2018). The perfusion workflow and adhesion quantification was the same as described above, save adhesion by fluorescent LS174T cells being imaged using a fluorescein isothiocyanate filter (excitation bandpass 475-492 nm, emission bandpass 505-535 nm) with a Chroma Technology 100W PhotoFluor mercury lamp with same microscope using an exposure time of 200 ms.

Quantification of Adhesive Cell Behavior

An adhering cell was defined as one that was seen to exhibit horizontal translation at a velocity substantially slower than the non-interacting cells, e.g. those transiting the imaging field of view at the calculated free fluid velocity as well as cell velocities observed when perfused over unfunctionalized channels. Individual cell velocities over 30 sec intervals were quantified using ImageJ with a manual particle tracking plugin.

Statistical Analysis

Statistical significance was defined as $p<0.05$ following one- or two-way ANOVA and post hoc analysis or linear regression using the analysis tools in Graphpad Prism 8.

Supplemental Figures

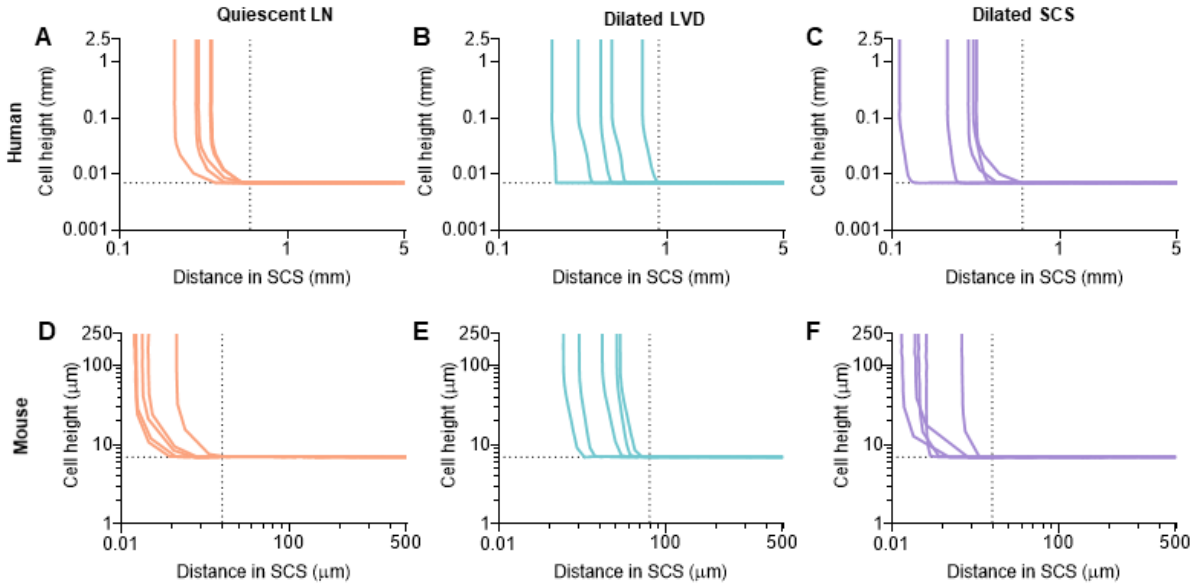

Figure S1. Computationally modelled trajectories of cells entering the LN SCS, related to Figures 2 and 3. COMSOL cell trajectory simulations using (A-C) human or (D-F) mouse LN parameters showing the position of the center of a cell of diameter 14 μm as it moves from the afferent lymphatic vessel into the SCS. Each colored line represents the trajectory of a single cell with a randomized radial starting location at the top of the afferent vessel. Dashed line on y-axis at a height of 7 μm, indicating the cell has settled to the bottom of the SCS floor. Dashed line on x-axis represent afferent vessel radius of (A,C) 0.6 mm (quiescent afferent LVD, human), (B) 0.9 mm (dilated LVD, human), (D,F) 40 μm (quiescent LVD, mouse), (E) 80 μm (dilated LVD, mouse).

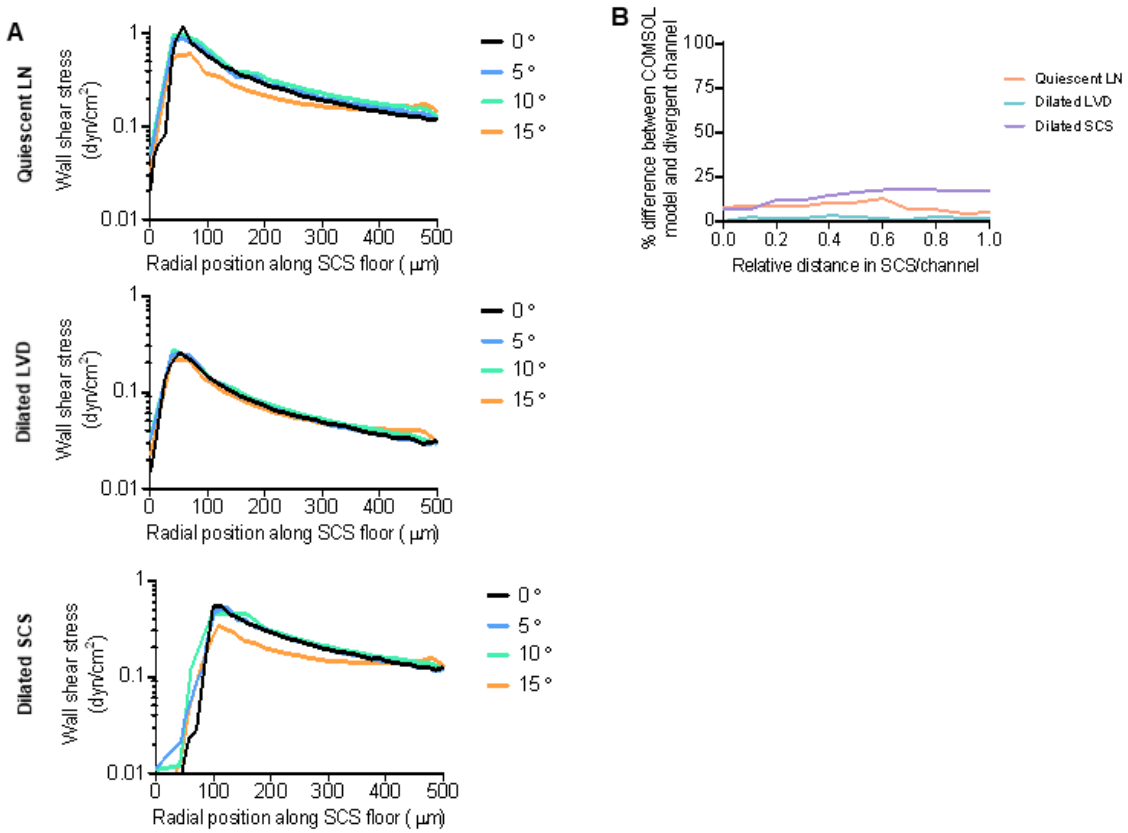

Figure S2. Computationally modelled effects of LN curvature effects on WSS and percent difference between COMSOL and divergent experimental flow model WSS profiles, related to Figures 2 and 3. (A) WSS levels predicted by COMSOL laminar fluid flow simulations through quiescent LNs (top), LNs with a dilated LVDs (middle), or LNs with a dilated SCS (bottom) with varying degrees of SCS curvature. (B) Percent difference between COMSOL and microfluidic experimental flow model WSS profiles.

Microfluidic model	Perfusion flow rate (µl/min)	WSS range (dyn/cm²)	Model LVD (µm)	Model SCS H (µm)
Quiescent LN	34.7	1 – 0.167	1.2	50
Dilated LVD	21.5	0.62 – 0.11	1.2	100
Dilated SCS	9.7	0.28 – 0.04	1.8	50

Table S1, related to Figure 3. Perfusion conditions used to model literature reported parameters human LNs.

Channel position (cm)	0	0.5	1	1.5	2	2.5	3	3.5	4
Microfluidic model	Wall Shear Stress (dyn/cm²)								
Quiescent LN	1.000	0.545	0.437	0.305	0.278	0.212	0.205	0.184	0.167
Dilated LVD	0.620	0.338	0.244	0.189	0.157	0.132	0.115	0.112	0.110
Dilated SCS	0.280	0.153	0.110	0.085	0.071	0.060	0.052	0.046	0.040

Table S2, related to Figure 3. WSS levels along the length of the divergent channel at different flow rates based on COMSOL simulations of human LN parameters.

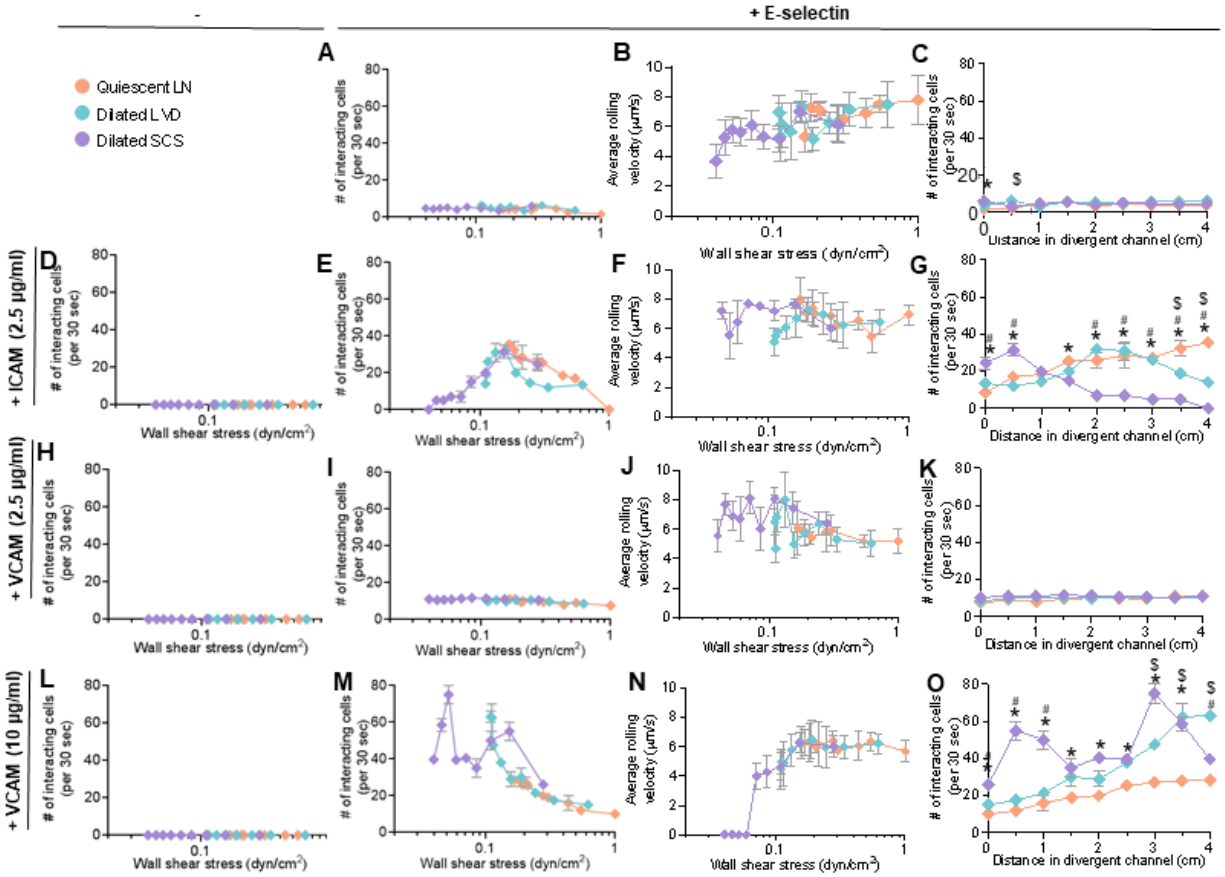

Figure S3. The WSS dependency of PANC-1 colon carcinoma cell adhesion in LN SCS-mimicking flow fields and microenvironments is altered by altered flow profiles predicted to result from LVD and SCS dilation, related to Figures 6 and 7. The number and average rolling velocity of PANC-1 cells adhering in flow in divergent channels functionalized with (A-C) 2.5 µg/mL E-selectin alone, (D) 2.5 µg/mL ICAM alone, (E-G) 2.5 µg/mL E-selectin + 2.5 µg/mL ICAM, (H) 2.5 µg/mL VCAM alone, (I-K) 2.5 µg/mL E-selectin + 2.5 µg/mL VCAM, (L) 10 µg/mL VCAM, or (M-O) 2.5 µg/mL E-selectin + 10 µg/mL VCAM. Statistical analysis by two-way ANOVA with post-hoc analysis between points at each channel position. $p < 0.05$ between: $ quiescent LN and dilated LVD, * quiescent LN and dilated SCS, and # dilated LVD and dilated SCS.

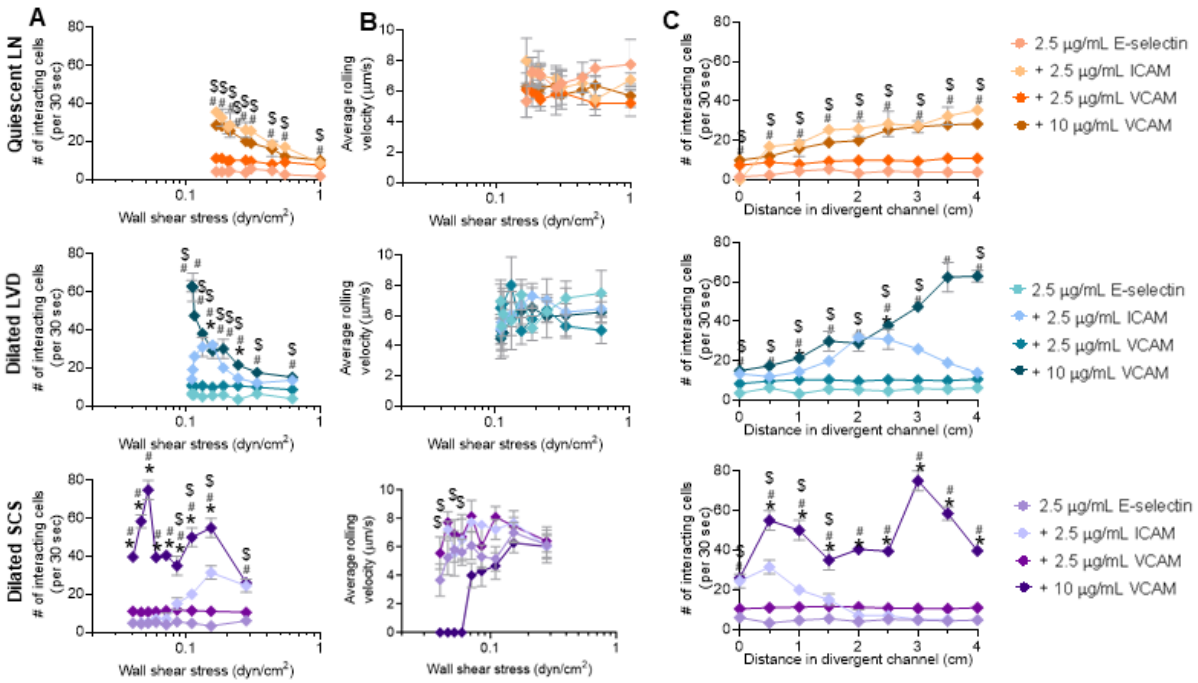

Figure S4. Co-presentation of adhesion molecules alters the WSS dependency of PANC-1 cell adhesion in flow, related to Figures 6 and 7. The number (A,C) and average rolling velocity (B) of PANC-1 cells adhering to E-selectin alone or when co-presented with ICAM or VCAM in flow regimes modelled after a quiescent LN (top row), LN with a dilated LVD (middle row), or LN with a dilated SCS (bottom row). Statistical analysis by unpaired t-test between points at each WSS or channel position. $p < 0.05$ between: $ E-selectin vs. E-selectin + 2.5 μg/mL ICAM, * E-selectin vs. E-selectin + 2.5 μg/mL VCAM, and # E-selectin vs. E-selectin + 10 μg/mL VCAM.

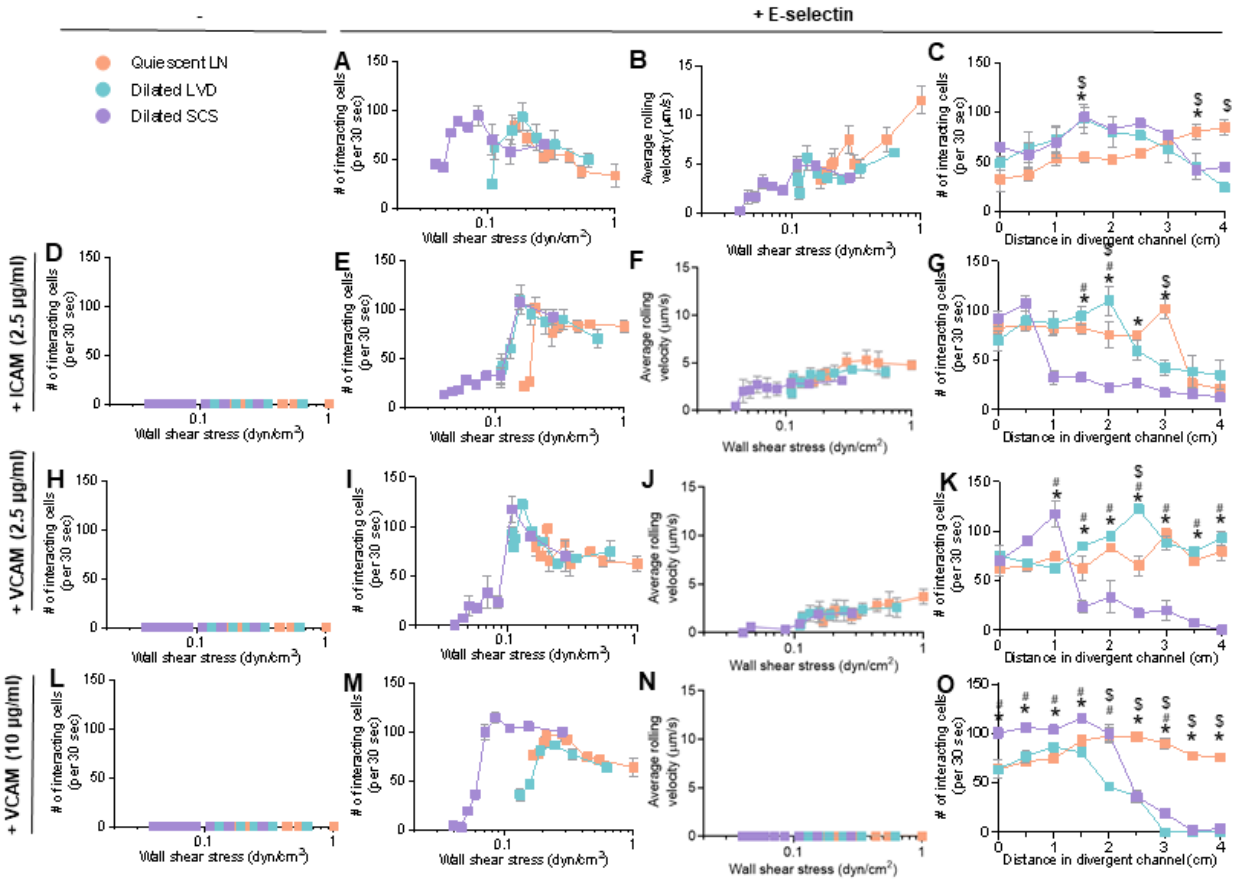

Figure S5. The WSS dependency of THP-1 colon carcinoma cell adhesion in LN SCS-mimicking flow fields and microenvironments is altered by altered flow profiles predicted to result from LVD and SCS dilation, related to Figures 6 and 7. The number and average rolling velocity of THP-1 cells adhering in flow in divergent channels functionalized with (A-C) 2.5 µg/mL E-selectin alone, (D) 2.5 µg/mL ICAM alone, (E-G) 2.5 µg/mL E-selectin + 2.5 µg/mL ICAM, (H) 2.5 µg/mL VCAM alone, (I-K) 2.5 µg/mL E-selectin + 2.5 µg/mL VCAM, (L) 10 µg/mL VCAM, or (M-O) 2.5 µg/mL E-selectin + 10 µg/mL VCAM. Statistical analysis by two-way ANOVA with post-hoc analysis between points at each channel position. $p < 0.05$ between: $ quiescent LN and dilated LVD, * quiescent LN and dilated SCS, and # dilated LVD and dilated SCS.

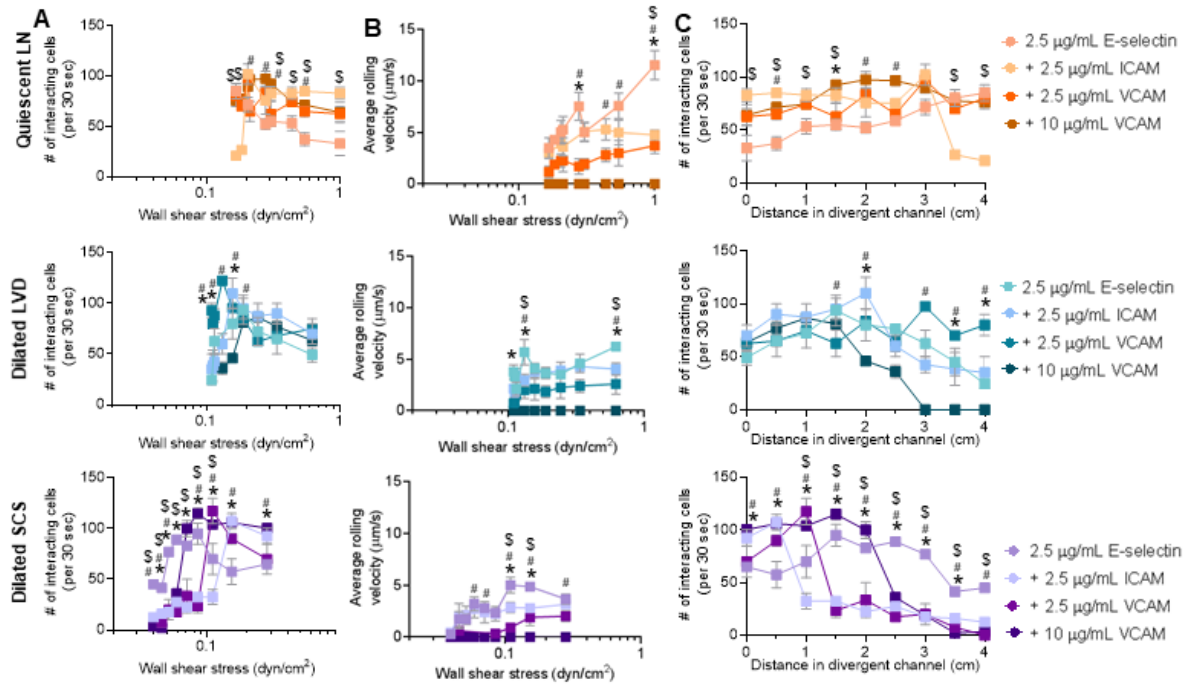

Figure S6. Adhesion molecule co-presentation alters WSS dependency of THP-1 adhesion in flow, related to Figures 6 and 7. The number (A,C) and average rolling velocity (B) of THP-1 cells adhering to E-selectin alone or when co-presented with ICAM or VCAM in flow regimes modelled after a quiescent LN (top row), LN with a dilated LVD (middle row), or LN with a dilated SCS (bottom row). Statistical analysis by two-way ANOVA with post-hoc analysis between points at each WSS or channel position. $p < 0.05$ between: $ E-selectin vs. E-selectin + 2.5 μg/mL ICAM, * E-selectin vs. E-selectin + 2.5 μg/mL VCAM, and # E-selectin vs. E-selectin + 10 μg/mL VCAM.

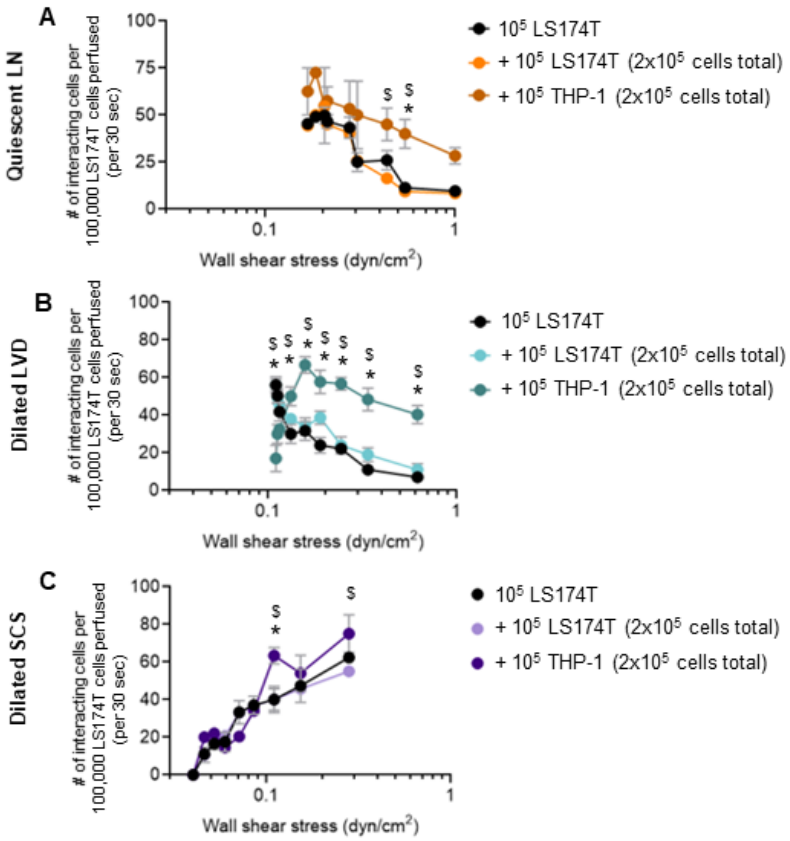

Figure S7. Increased adhesion by LS174T cells co-perfused with THP-1 cells is not due to steric interference, related to Figure 8. The number of LS174T cells mediating adhesion to E-selectin in flow when perfused alone (a total of 10^5 LS174T cells perfused) or during co-perfusion with either an additional 10^5 LS174T cells (total of $2x10^5$ LS174T cells perfused) or 10^5 THP-1 cells (total $2x10^5$ cells) in flows modeled after a (A) healthy LN, (B) LN with a dilated LVD, or (C) a LN with a dilated SCS. To adjust for differences in the number of perfused LS174T cell during a single cell perfusion of $2x10^5$ LS174T cells, the total number of interacting cells at each measured WSS was divided by two. Statistical analysis by two-way ANOVA with post-hoc analysis between points at each WSS. $p < 0.05$ between: \$ 10^5 LS174T vs + 10^5 LS174T, * 10^5 LS174T vs + 10^5 THP-1, and # + 10^5 LS174T vs. + 10^5 THP-1.